Cell Reports

Article

Cell-to-cell variability in JAK2/STAT5 pathway components and cytoplasmic volumes defines survival threshold in erythroid progenitor cells

Graphical Abstract

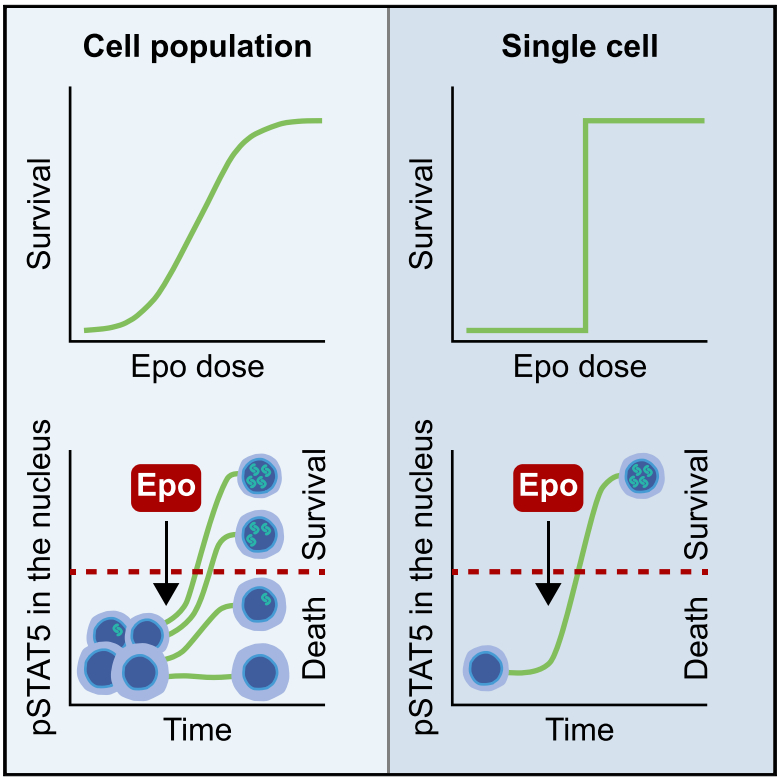

Authors

Lorenz Adlung, Paul Stapor, Christian Tönsing, ..., Ursula Klingmüller, Jan Hasenauer, Marcel Schilling

Correspondence

jeti@fdm.uni-freiburg.de (J.T.), u.klingmueller@dkfz.de (U.K.), jan.hasenauer@uni-bonn.de (J.H.), m.schilling@dkfz.de (M.S.)

In brief

Adlung et al. analyze cell-to-cell variability in the response of precursors of red blood cells to the hormone Epo. Experimental data and mathematical modeling show that the survival of an individual cell depends on the amount of signal transduction proteins and the size of the cell.

Highlights

- Mathematical modeling enables integration of heterogeneous data
- Single-cell modeling captures a binary decision process
- Multiple sources of cell-to-cell variability exist in erythroid progenitor cells
- Minimal amount of active STAT5 is sufficient for erythroid progenitor cell survival

Adlung et al., 2021, Cell Reports *36*, 109507
August 10, 2021
https://doi.org/10.1016/j.celrep.2021.109507

CellPress

Cell Reports

CellPress
OPEN ACCESS

Article

Cell-to-cell variability in JAK2/STAT5 pathway components and cytoplasmic volumes defines survival threshold in erythroid progenitor cells

Lorenz Adlung,[1,2,3,10] Paul Stapor,[4,5,10] Christian Tönsing,[6,7,10] Leonard Schmiester,[4,5] Luisa E. Schwarzmüller,[1] Lena Postawa,[1] Dantong Wang,[4,5] Jens Timmer,[6,7,*] Ursula Klingmüller,[1,8,*] Jan Hasenauer,[4,5,9,*] and Marcel Schilling[1,11,*]

[1]Division Systems Biology of Signal Transduction, German Cancer Research Center (DKFZ), 69120 Heidelberg, Germany
[2]Department of Medicine, University Medical Center Hamburg-Eppendorf, 20246 Hamburg, Germany
[3]Hamburg Center for Translational Immunology (HCTI), University Medical Center Hamburg-Eppendorf, 20246 Hamburg, Germany
[4]Helmholtz Zentrum München - German Research Center for Environmental Health, Institute of Computational Biology, 85764 Neuherberg, Germany
[5]Technische Universität München, Center for Mathematics, Chair of Mathematical Modeling of Biological Systems, 85748 Garching, Germany
[6]Institute of Physics and Freiburg Center for Data Analysis and Modelling (FDM), University of Freiburg, 79104 Freiburg, Germany
[7]CIBSS–Centre for Integrative Biological Signalling Studies, University of Freiburg, 79104 Freiburg, Germany
[8]Translational Lung Research Center (TLRC), Member of the German Center for Lung Research (DZL), 69120 Heidelberg, Germany
[9]Faculty of Mathematics and Natural Sciences, University of Bonn, 53113 Bonn, Germany
[10]These authors contributed equally
[11]Lead contact
*Correspondence: jeti@fdm.uni-freiburg.de (J.T.), u.klingmueller@dkfz.de (U.K.), jan.hasenauer@uni-bonn.de (J.H.), m.schilling@dkfz.de (M.S.)
https://doi.org/10.1016/j.celrep.2021.109507

SUMMARY

Survival or apoptosis is a binary decision in individual cells. However, at the cell-population level, a graded increase in survival of colony-forming unit-erythroid (CFU-E) cells is observed upon stimulation with erythropoietin (Epo). To identify components of Janus kinase 2/signal transducer and activator of transcription 5 (JAK2/STAT5) signal transduction that contribute to the graded population response, we extended a cell-population-level model calibrated with experimental data to study the behavior in single cells. The single-cell model shows that the high cell-to-cell variability in nuclear phosphorylated STAT5 is caused by variability in the amount of Epo receptor (EpoR):JAK2 complexes and of SHP1, as well as the extent of nuclear import because of the large variance in the cytoplasmic volume of CFU-E cells. 24–118 pSTAT5 molecules in the nucleus for 120 min are sufficient to ensure cell survival. Thus, variability in membrane-associated processes is sufficient to convert a switch-like behavior at the single-cell level to a graded population-level response.

INTRODUCTION

Signal transduction has been intensively studied in the past decades at the cell population level with immunoblotting and bulk gene-expression analyses. However, information processing is highly dynamic and occurs at the single-cell level with considerable cell-to-cell variability (Taniguchi et al., 2010), which can either be beneficial or harmful (Raj and van Oudenaarden, 2008); e.g., cell-to-cell variability can improve the robustness of signal transduction (Paszek et al., 2010) but lead to incomplete growth inhibition of tumor cells (Niepel et al., 2009). It has been reported that, although cell-to-cell variability is fundamental to most molecular processes in cells, quantitative assessment of how that influences intracellular information processing is almost completely lacking (Pelkmans, 2012).

The Janus kinase 2/signal transducer and activator of transcription 5 (JAK2/STAT5) signal transduction pathway serves as a paradigm in mediating the survival of erythroid progenitor cells (Socolovsky et al., 2001). At the stage of colony forming unit erythroid (CFU-E), cells are highly sensitive to erythropoietin (Epo) (Nijhof and Wierenga, 1983) and respond in a graded input-output relationship (Koulnis et al., 2014) to ensure robust physiological production of erythrocytes. Rapid signal transduction is facilitated by binding of Epo to its cell-surface receptor, the EpoR, inducing gene expression (Swameye et al., 2003) and CFU-E survival (Bachmann et al., 2011). The Epo-EpoR complex activates the receptor-associated Janus kinase, JAK2, which phosphorylates the cytoplasmic tail of the EpoR on multiple tyrosine residues (Klingmüller et al., 1996). STAT5 is recruited to the phosphorylated receptor complex and is, in turn, phosphorylated by JAK2 (Gouilleux et al., 1995). Phosphorylated STAT5 (pSTAT5) molecules form dimers (Boehm et al., 2014), translocate to the nucleus, and induce the expression of anti-apoptotic genes, e.g., *Bcl2l1* for immediate control of cell survival

(Socolovsky et al., 1999). Other STAT5 target genes include *Cish* (Yoshimura et al., 1995) and *Socs3* (Sasaki et al., 2000), which encode the negative-feedback regulators cytokine-inducible SH2-domain-containing protein (CIS) and suppressor of cytokine signaling 3 (SOCS3), which attenuate signal transduction. The SH2-domain-containing protein tyrosine phosphatase 1 (SHP1) is a cytosolic protein that is recruited to the activated receptor via its SH2 domain (Neel et al., 2003), causing dephosphorylation of JAK2 leading to the termination of signal transduction (Klingmüller et al., 1996). However, it remained elusive how the gradual Epo-induced increase in STAT5 phosphorylation and survival of CFU-E cells at the cell-population level relates to the switch-like, all-or-none survival decision that occurs in an individual cell.

Here, we report the development of a population-average mathematical model of the Epo-induced JAK2/STAT5 signal transduction pathway in primary murine CFU-E cells that captures cellular population-average data. This model, in combination with flow cytometric analyses of STAT5 and pSTAT5, is used to create a mixed-effect mathematical model of pathway activation at the single-cell level. The analysis of the single-cell model suggests that a high variability in the amounts of the EpoR:JAK2 complex and the phosphatase SHP1 and in the nuclear translocation rates of STAT5 contributes to the detected high variability in nuclear pSTAT5. With this approach, we identify a relative threshold of nuclear pSTAT5 that decides survival in CFU-E cells, and we elucidate the mechanisms converting the switch-like survival decision in individual CFU-E cells to a graded response at the population level. These results are consistent with the concept established by an information theoretic approach that variability at the single-cell level increases the accuracy of information transfer at the cell-population level (Suderman et al., 2017).

RESULTS

Cell-to-cell variability of phosphorylated STAT5 in primary erythroid progenitor cells

The key intracellular integrator of Epo-induced survival-signal transduction in CFU-E cells is the latent transcription factor STAT5, which is activated by tyrosine phosphorylation (pSTAT5). To experimentally evaluate the expression of STAT5, we stimulated CFU-E cells for 15 min with a broad range of Epo doses that support cell survival (Bachmann et al., 2011) (Figure S1) and monitored the expression of total STAT5 and of Epo-induced phosphorylation of STAT5 by flow cytometry (Figures 1A–1E). In unstimulated CFU-E cells, total STAT5 was detected with a mean fluorescence intensity of 0.49 and a standard deviation (SD) of 0.10, with major contributions of non-specific binding of the secondary antibody (Figure 1A). Upon stimulation with increasing doses of Epo, the mean fluorescence intensity of total STAT5 varied between 0.45 and 0.48, showed an SD of 0.10–0.11, and was, thus, rather unaffected by Epo. The flow cytometric detection of pSTAT5 yielded, in the unstimulated situation, a mean fluorescence intensity of 0.23 and a SD of 0.10, again, with major contributions of the secondary antibody alone (Figure 1B). However, upon stimulation with 0.16 U/mL of Epo, the mean fluorescence intensity measured for pSTAT5 shifted to a higher mean value (0.25) and was distributed more broadly (SD of 0.12) (Figure 1C). This effect was even more pronounced upon stimulation with 4 U/mL Epo, with a mean fluorescence intensity of 0.32 and an SD of 0.16 (Figure 1E), which remained the same upon adding even higher Epo doses (Figure 1D). Although the fraction of surviving CFU-E cells for the respective Epo concentration, as interpolated from our previously reported data (Bachmann et al., 2011), increased in a graded fashion (Figure S1), the mean fluorescence intensities and SDs of total STAT5 did not change with increasing Epo doses. On the contrary, for pSTAT5, we observed a gradual increase in the mean fluorescence intensity that saturated similar to the CFU-E cell survival at a concentration of 4 U/mL Epo. Interestingly, the SD observed for pSTAT5 was considerably larger than that for total STAT5 and showed an increase in response to rising Epo doses that correlated with the survival responses (Figure 1D).

Thus, we concluded that the cell-to-cell variability in the expression of total STAT5 alone was not sufficient to explain the Epo dose-dependent increase in the variance of the key integrator of survival signaling pSTAT5.

Dynamical modeling of Epo-induced JAK2/STAT5 signal transduction at the population level

To identify pathway components and reaction rates in the JAK2/STAT5 signaling pathway that vary from cell to cell and could cause the observed variability in pSTAT5, we developed a workflow for an in-depth analysis of cell-to-cell variability by mechanistic mathematical modeling (Figure 1F).

To establish a mechanistic mathematical model that describes the system on a population-average level, we used our model of the JAK2/STAT5 pathway (Bachmann et al., 2011) (Figure 2A). So far, model calibration has been performed with quantitative immunoblotting data, quantitative mass spectrometry, and qRT-PCR data, which assess cell-population averages. However, flow cytometry offers, in addition, information on the distribution of the fluorescence intensity across the cell population, which links to the single-cell level. To calibrate the parameters of our population-average model, we collected quantitative data acquired in CFU-E cells with a wide variety of experimental approaches and conditions:

(1) Quantitative immunoblotting analysis of total cell lysates for pSTAT5 and total STAT5 (tSTAT5) and of cytoplasmic lysates for pEpoR, pJAK2, CIS, SOCS3, and SHP1 served as a readout to determine the average Epo-induced activation of the JAK2/STAT5 pathway (Figures 2B and S2: B5, B7, C5-C6, D1–D4, D7–E4, E6–F2, F5–G4, G6, H7, K1–K4, and K6 and K7).
(2) Targeted mass spectrometry using one-source peptide/phosphopeptide ratio standards (Boehm et al., 2014) allowed us to determine relative average amounts of pSTAT5 in response to Epo stimulation (Figures 2C and S2: L1 and L2).
(3) Cell fractionation experiments, separating the cytoplasm and the nucleus, provided access to the average dynamics of pSTAT5 localization (Figures 2D, 2E, and S2: B1–B4, B6, C1–C4, C7, D5, D6, E5, F3, F4, G5, G7, H6, and K5).

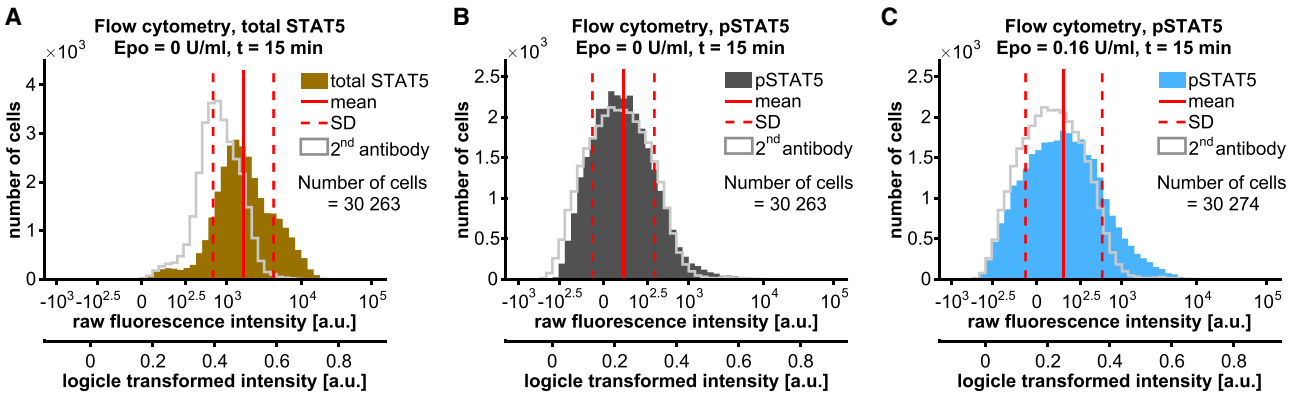

D

Epo dose	Survival at t = 20 h	Flow cytometry dose-response at t = 15 min			
		total STAT5		pSTAT5	
	[%]	logicle transformed intensity [a.u.]		logicle transformed intensity [a.u.]	
[U/ml]	mean	mean	SD	mean	SD
0	6.9	0.49	0.10	0.23	0.10
0.0064	17.7	0.47	0.10	0.23	0.11
0.032	54.3	0.47	0.10	0.23	0.11
0.16	77.9	0.46	0.10	0.25	0.12
0.8	81.2	0.45	0.10	0.28	0.14
4	82	0.46	0.10	0.32	0.16
20	82	0.48	0.10	0.33	0.16
100	82	0.46	0.11	0.33	0.16

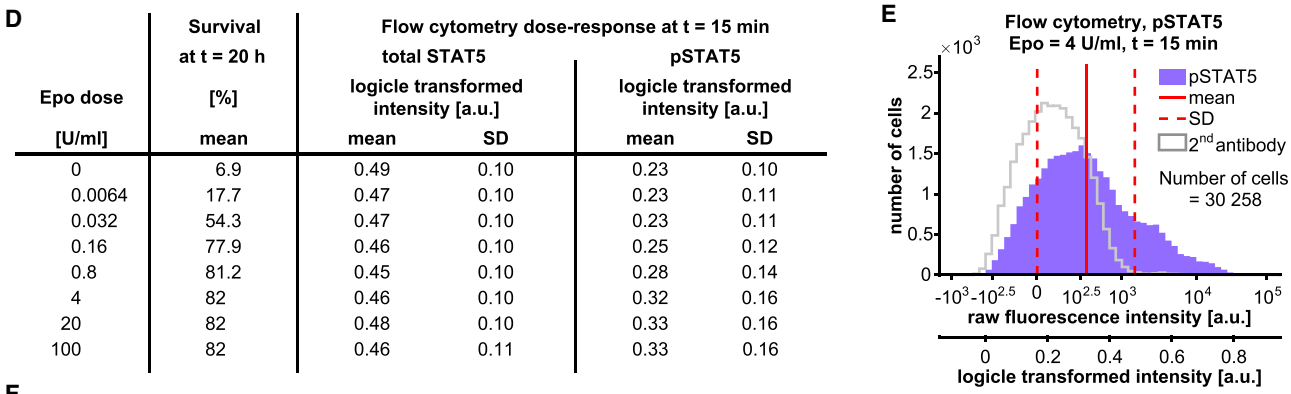

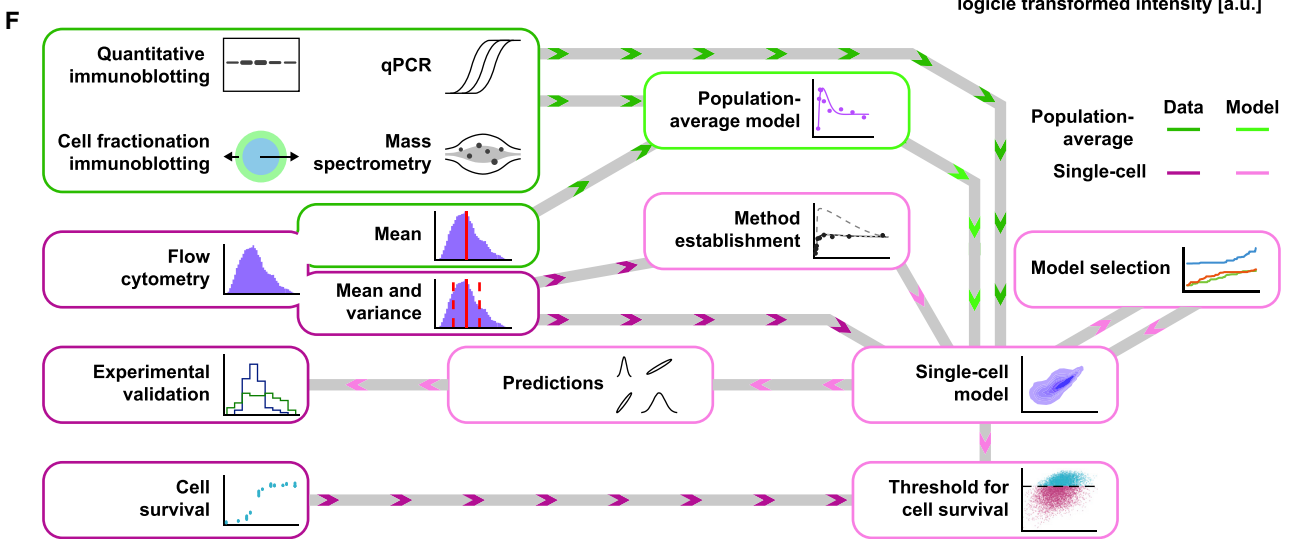

Figure 1. Cell-to-cell variability in total and phosphorylated STAT5

(A–E) Unstimulated growth-factor-depleted CFU-E cells were fixed, permeabilized, and intracellularly stained with goat anti-STAT5 primary antibody and anti-goat fluorescein isothiocyanate (FITC) secondary antibody (brown) or only the secondary antibody (gray line) (A). Growth-factor-depleted CFU-E cells were (B) unstimulated or were stimulated with (C) 0.16 U/mL Epo or (E) 4 U/mL Epo for 15 min and were subjected to intracellular staining with rabbit anti-pSTAT5 antibody and with anti-rabbit APC secondary antibody: dark gray (unstimulated), blue (0.16 U/mL Epo), purple (4 U/mL Epo), or secondary antibody only (gray line). Raw fluorescence intensities are plotted in a bi-exponential manner, and in each panel, the corresponding logicle scale is indicated. (D) Growth-factor-depleted CFU-E cells were stimulated for 20 h with the indicated Epo concentrations, and the corresponding fraction of surviving CFU-E cells was extrapolated (Figure S1) based on previously published data (Bachmann et al., 2011). For each of these Epo concentrations, the extracted mean and standard deviation (SD) of the flow cytometric measurements of total STAT5 and pSTAT5 transformed to the logicle scale are displayed.

(F) Schematic workflow figure for the experiments and mathematical models is shown. Dark green corresponds to population-average data and dark pink to single-cell data. The population-average mathematical model is shown in light green, and mathematical approaches and models describing single-cell behavior are shown in light pink. Lines with arrows denote information flow.

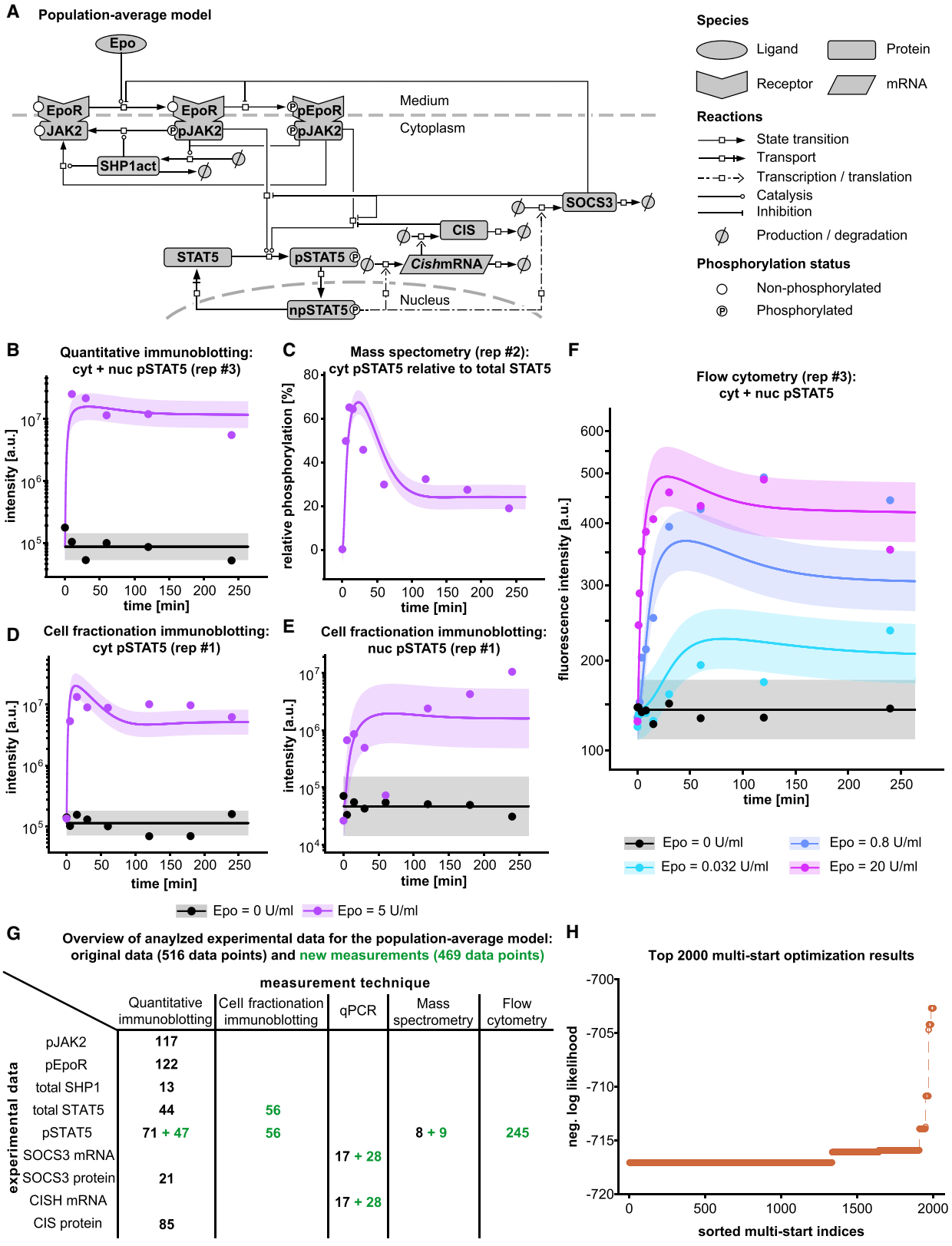

G

Overview of anaylzed experimental data for the population-average model: original data (516 data points) and new measurements (469 data points)

experimental data \ measurement technique	Quantitative immunoblotting	Cell fractionation immunoblotting	qPCR	Mass spectrometry	Flow cytometry
pJAK2	117				
pEpoR	122				
total SHP1	13				
total STAT5	44	56			
pSTAT5	71 + 47	56		8 + 9	245
SOCS3 mRNA			17 + 28		
SOCS3 protein	21				
CISH mRNA			17 + 28		
CIS protein	85				

(legend on next page)

(4) qRT-PCR experiments (Figure S2: I5–I7 and J1–J7) revealed the induction dynamics of the transcriptional feedbacks.
(5) The mean fluorescence intensities of the flow cytometry data on pSTAT5 provided time and Epo-dose resolved information on the average pSTAT5 concentration in the cell population (Figures 2F and S2: A1–A3 and B7).

Altogether, a curated dataset was assembled of 516 published data points (Bachmann et al., 2011) and 469 newly acquired data points, providing information on the average dynamic behavior of the JAK2/STAT5 pathway in the cell population (Figure 2G).

The resulting population-average model (Figure 2A) differed from the previously published model in three aspects: (1) SHP1 activation was simplified, (2) SOCS3 transcription and translation processes were summarized, and (3) the CIS transcriptional delay was shortened. Calibrating the reduced model to the experimental data showed a favorable convergence (Raue et al., 2013b) during parameter optimization (Figure 2H), good agreement (see Figure S2), and high correlation ($\rho = 0.978$; see Figures S4A and S4B) between the experimental data and the model output for the best fit. The profile-likelihood calculation revealed that 19 of 21 of the estimated dynamic parameters of the population-average model are practically identifiable at a confidence level of 95%, and all 21 parameters are practically identifiable at a confidence level of 68% (Figure S3).

To conclude, we calibrated a population-average model for the JAK2/STAT5 pathway in CFU-E cells that is capable of accurately describing the dynamics of pathway activation in these cells.

Mathematical modeling reveals that abundance of pathway components and nucleocytoplasmic transport rates determine cell-to-cell variability of pSTAT5

To describe Epo-induced JAK2/STAT5 signal transduction at the single-cell level, we compared different approximation methods to enable parameter estimation in single-cell models. To reduce computational costs, we first approximated the mean and the covariance by sigma points, which resulted in low accuracy (Figure 3A). Next, we tried a Dirac-mixture distribution, which allowed high accuracy in describing cell-to-cell variability (Figure 3B) and was about 250 times faster than simulating the corresponding Monte-Carlo-based trajectories (Figure 3C). Nevertheless, parameter estimation using 400 multi-start local optimizations required approximately 10,000 h of computation time for the single-cell model, compared with approximately 85 h for the population-average model.

To identify the relevant components and reactions and to quantify their contribution to the variability of pSTAT5, we established three nested, single-cell models (single-cell models 1–3; Figure 4A). For single-cell model 1, we assumed cell-to-cell variability in the initial amounts of the EpoR:JAK2 complex, SHP1, and total STAT5, as well as the offset parameter for the basal STAT5 phosphorylation. To account for interdependencies among these random effects (i.e., parameters varying across individual cells), the full covariance matrix was estimated (Figure 4B, blue). Single-cell model 2 was extended by estimating the nucleocytoplasmic cycling rates of STAT5 to vary among individual cells. Interdependencies were only considered between import and export rate constants but not with other random effects to limit the complexity of the covariance matrix (Figure 4B, green). Single-cell model 3 was extended by estimating the input Epo to vary among cells but independent of all other random effects (Figure 4B, orange). Models were calibrated to the means and variances of total STAT5 and pSTAT5 as measured by flow cytometry (Figures 4C–4E) and showed good convergence (Figure 4F). Model selection revealed the best balance between goodness-of-the-fit and model complexity for single-cell model 2, which considers cell-to-cell variability for the initial amount of EpoR, SHP1, and total STAT5, as well a cell-specific offset for pSTAT5, and cell-specific nucleocytoplasmic import and export rate constants of STAT5, as most suitable to the comprehensive experimental data. Thus, we demonstrated that variability in the protein abundance of pathway components and in nucleocytoplasmic translocation of STAT5 had a major influence on Epo-induced pSTAT5 in individual CFU-E cells and proceeded with that model structure.

Prediction and experimental validation of cell-to-cell variability in protein abundance and cell geometry

To validate our parameter estimation method based on Dirac-mixture distributions, we compared the single-cell JAK2/STAT5 model output of the distributions of pSTAT5 and total STAT5 to the flow cytometry data for the time-course at 4 U/mL Epo and observed a good agreement of the mean (Figure 5A, circles) and covariances (Figure 5A, crosses). We further compared the measured population densities of total STAT5 versus pSTAT5 at each time point, which have not been considered for parameter estimation, but were comparable with the simulations (Figure 5A, shades of purple).

To identify the pathway components and reactions rates responsible for the cell-to-cell variability of pSTAT5, we plotted the fitted variances and covariances of the random effects

Figure 2. Modeling of population-average dynamics

(A) Process diagram of the population-average JAK2/STAT5 model according to Systems Biology Graphical Notation (SBGN) (Le Novère et al., 2009)

(B–F) Illustrative experimental data (filled circles) and model simulations (solid lines) for pSTAT5 (see Figure S2 for complete dataset with the full range of Epo doses, with all replicates and observed model outputs). Data shown were generated by (B) quantitative immunoblotting from whole-cell lysates, (C) quantitative mass spectrometry from cytoplasmic lysates, (D and E) quantitative immunoblotting from cytoplasmic and nuclear lysates upon cell fractionation experiments, and (F) population-average fluorescence intensities of pSTAT5 measured by flow cytometry (see Figure S2: A1–3 for all Epo doses).

(G) Summary of experimental data used for calibration of the population-based mathematical model. The number of data measurements in the published dataset (Bachmann et al., 2011) are given in black, and new measurements from this study are provided in green.

(H) Multi-start optimization results, shown as a likelihood waterfall plot (Raue et al., 2013b). The best 2,000 of 5,000 local optimization runs are shown, and plateaus indicate convergence to local or global optima. See Figure S3 for profile likelihood of estimated model parameters and Figures S4A and S4B for correlation of data and model output.

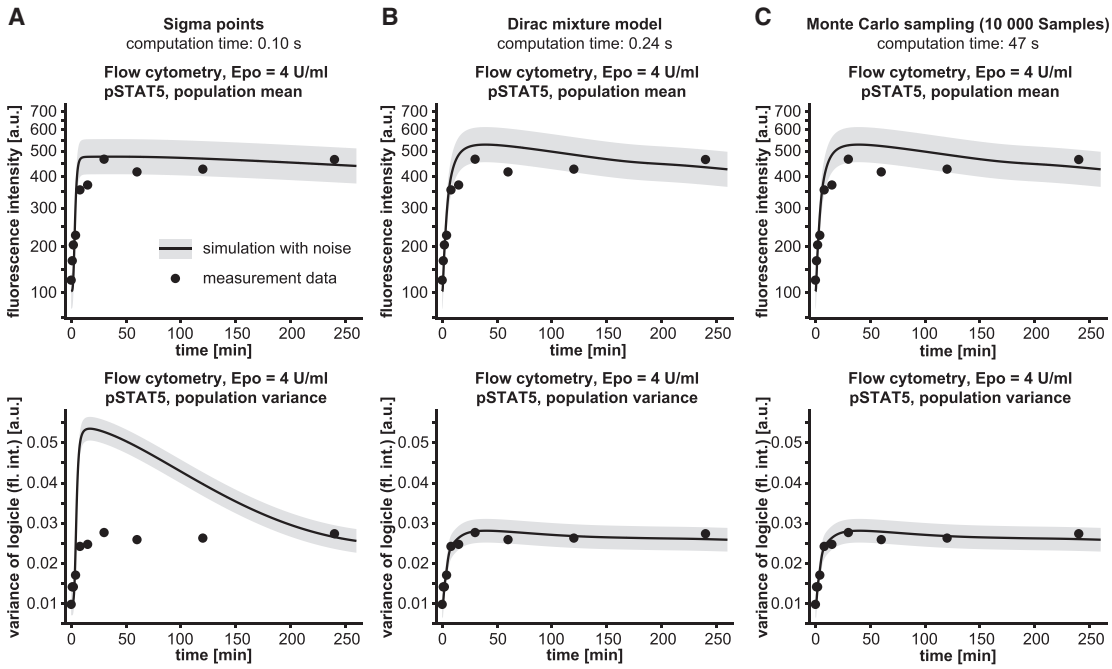

Figure 3. Modeling of population-average dynamics

(A–C) Exemplary model outputs of different approximation methods for the mean of the time-resolved flow cytometry experiment depicted in Figure 2F and the corresponding variance: (A) Sigma points, (B) Dirac-mixture distributions for the 42 Dirac points, and (C) a massive Monte Carlo sampling with 10,000 cells. Means (top panels) and variances (bottom panels) of pSTAT5 for the flow cytometry experiment are shown in Figure 2 for 4 U/mL Epo.

(Figure 5B). The mathematical model predicted higher variances for the membrane-associated EpoR:JAK2 complex and for SHP1 than for total STAT5. Additionally, the inferred covariance matrix revealed correlations between individual cellular states.

To experimentally verify the predicted high variances for SHP1 in CFU-E cells, we measured SHP1 by flow cytometry. Upon testing the staining procedure (Figure S6A), SHP1 and STAT5 were measured in unstimulated growth-factor-depleted CFU-E cells isolated from fetal mouse livers in five biological replicates (Figures S6B–S6F). In line with our model predictions, we observed a large coefficient of variation of 0.130 ± 0.005 for SHP1 and a significantly smaller coefficient of variation of 0.090 ± 0.004 for STAT5. The model also predicted that the cell-to-cell variability for the EpoR:JAK2 complex would be less than for SHP1. In the absence of suitable flow cytometry antibodies against the murine EpoR, CFU-E cells were isolated from fetal livers of knockin mice that express a GFPcre fusion protein controlled by the endogenous EpoR promoter (Heinrich et al., 2004). The GFP signal, revealing the cell-to-cell variability of the expression controlled by the endogenous EpoR promoter showed a rather small coefficient of variation of 0.039 ± 0.002 (n = 3).

The calibrated single-cell model of the JAK2/STAT5 pathway predicted the nuclear import and export rates of STAT5 to vary substantially between cells. Interestingly, the inferred variance for the nuclear import of pSTAT5 was larger than the inferred variance of the nuclear export of STAT5 (Figure 6A). We quantified this by the ratio of their coefficients of variation, which we assessed by simulating 1,000 *in-silico* populations with 100,000 CFU-E cells each. This yielded the following value:

$$\frac{\mathrm{CV}(\text{Import rate constant})}{\mathrm{CV}(\text{Export rate constant})} = 3.9 \pm 1.6.$$

Assuming the transport processes to be driven by diffusion, theoretical considerations (Bressloff, 2014) suggested that the average translocation times of STAT5 (proportional to the inverses of the translocation rate constants) should scale with the squared radius of the nucleic sphere and the squared thickness of the cytoplasmic shell (Figure 6B), respectively. As shown in Figure 6C, simulation of these diffusion processes as random-walks in three-dimensional (3D) structures, and computation of the dependence of expected translocation times of these two quantities (Figure 6C) confirmed that assumption.

To experimentally validate the prediction of this ratio of variability in the rate constants of STAT5 nuclear translocation, we measured the cytoplasmic and nuclear volumes of CFU-E cells. We stained the plasma membrane and the nucleus of CFU-E cells and reconstructed their 3D structure from confocal fluorescence microscope z stack images (Figure 6D). In agreement with the predictions of our single-cell JAK2/STAT5 model, the measured nuclear volume of CFU-E cells, which we considered as a proxy for the nuclear export rate constants, showed lower variance than the measured cytoplasmic volume, which we considered as a proxy for the thickness of the cytoplasmic shell and hence for the nuclear import constants (Figure 6E). Furthermore, we quantified the ratio of the coefficients of variation of the corresponding quantities to be as follows:

CellPress
OPEN ACCESS

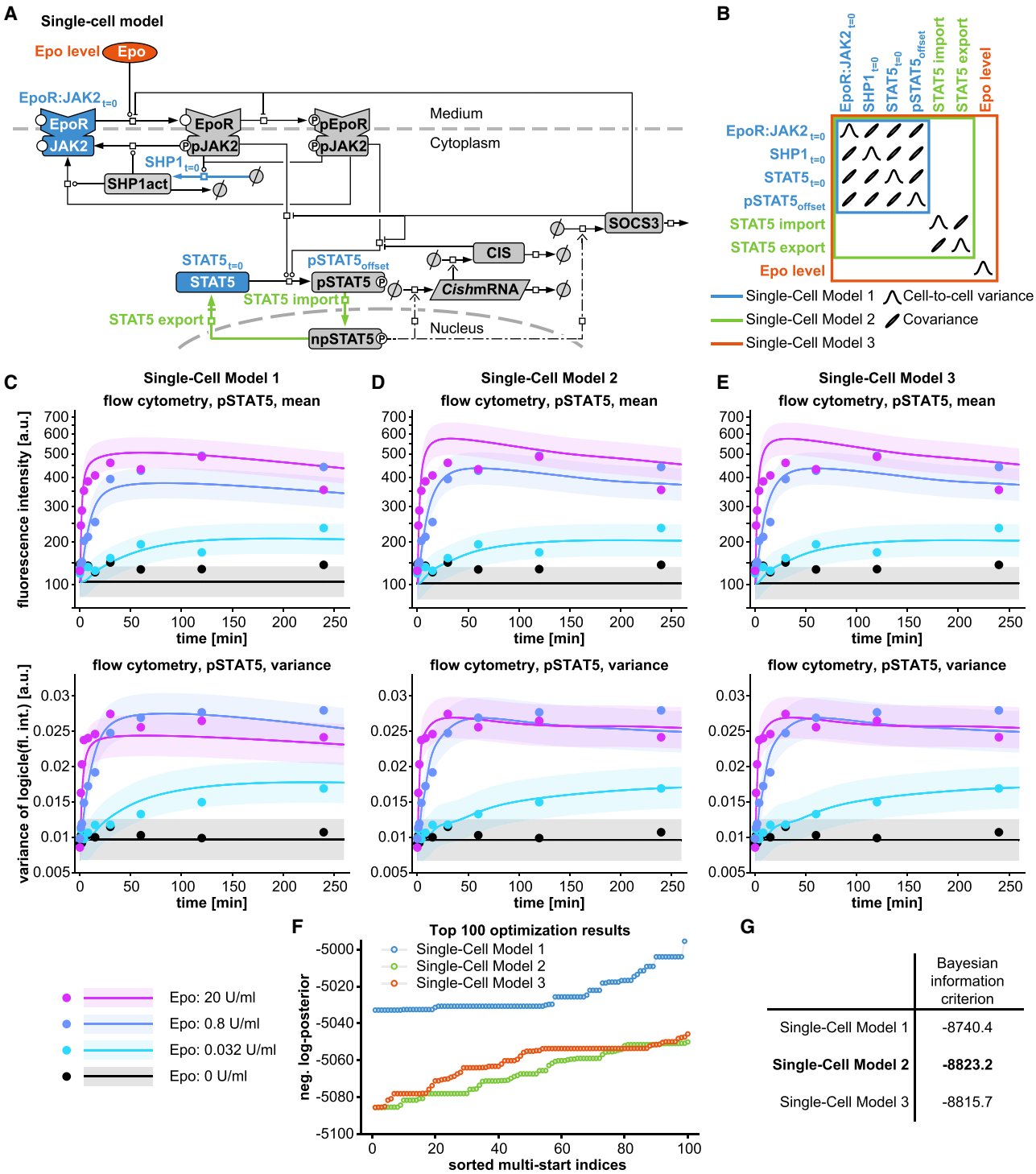

Figure 4. Dynamic mathematical JAK2/STAT5 pathway model describing cell-to-cell variability of phosphorylated STAT5

(A) The structure of the single-cell model of the JAK2/STAT5 pathway with putative sources of cell-to-cell variability of pSTAT5 (colored corresponding to the different models).

(B) Visualization of covariance matrix for the three candidate models.

(C–E) Experimental data (mean and variance of pSTAT5 from flow cytometry) and mixed-effect model outputs. See Figure S4 for correlation of data and model output and Figure S5 for full flow cytometry dataset and model output.

(F) Multi-start optimization results for candidate single-cell models. Best 100 of 400 local optimization runs are shown, and plateaus indicate convergence.

(G) Bayesian information criterion (BIC) values of the three candidate models.

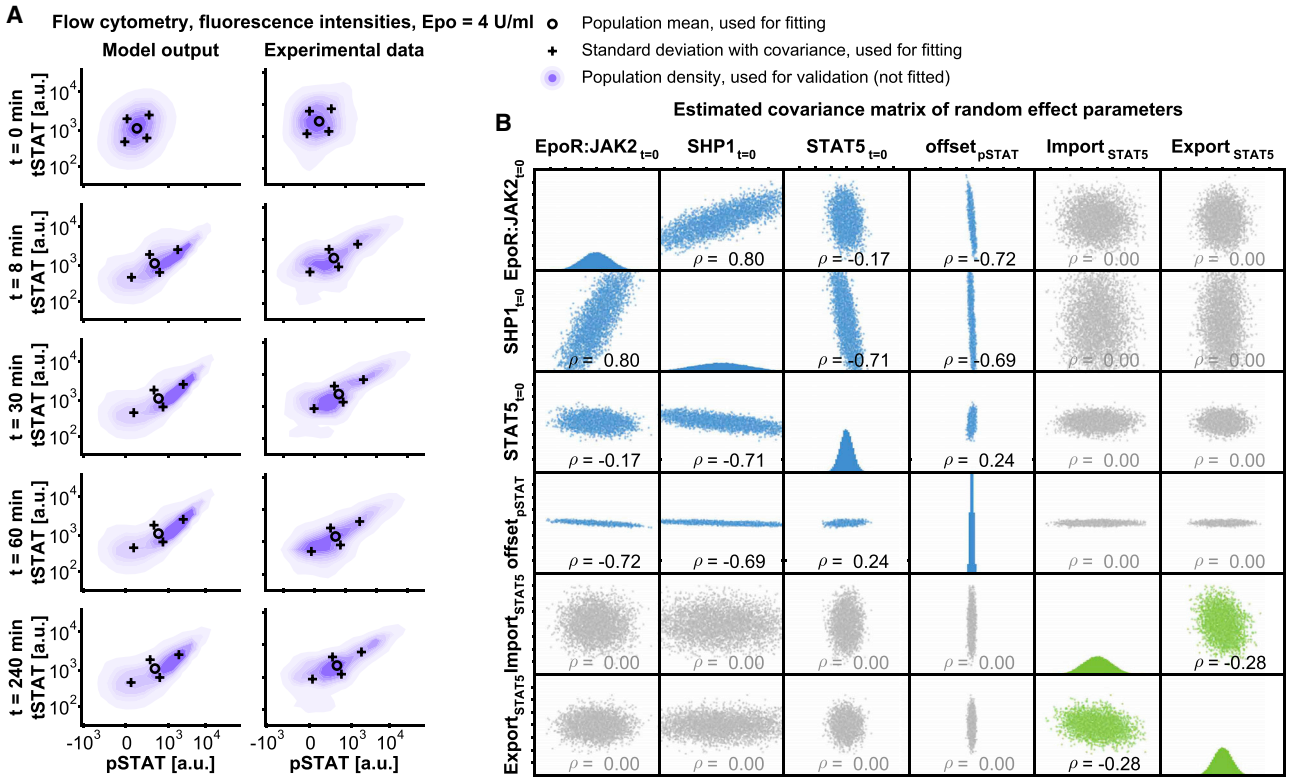

Figure 5. Model simulations of distributions of individual cellular states

(A) Experimental data and output of the single-cell JAK2/STAT5 model for a simulated population of 10,000 CFU-E cells of total STAT5 against pSTAT5. The mean and the covariances of the experimental data shown in Figure S5 were used for calibration of the single-cell model. Means of the model parameters depicted as circles and the covariances shown as crosses along the main axes of an ellipse are defined by the covariance structure at distances of one standard deviation. The experimentally determined distributions in a population of 10,000 CFU-E cells are shown as densities.

(B) Distributions and corresponding cross-correlations of random-effect parameters of the single-cell model.

$$\frac{\mathrm{CV}(\text{thickness of cytoplasmic shell}^{2})}{\mathrm{CV}(\text{radius of nucleus core}^{2})} = 3.1,$$

which was in line with our model prediction. In conclusion, we identified that, in addition to variability in the abundance of total STAT5, variability of the EpoR:JAK2 complex and SHP1 as well as of the nuclear import rate, which is a consequence of the large cell-to-cell variability of the cytoplasmic volumes, are responsible for the variability of pSTAT5.

Given the large influence of the cytoplasmic volumes on the cell-to-cell variability of pSTAT5, we hypothesized that, if the cellular geometry is a critical determinant of this variability, a simultaneous effect on the extent of the phosphorylation of other STAT family members that undergo nucleo-cytoplasmic cycling, such as STAT1 and STAT3, is to be expected. To examine whether pSTAT5 correlates with pSTAT1, we stained these molecules in CFU-E cells and detected by flow cytometry their concentration at the single-cell level. Although, in unstimulated CFU-E cells, both pSTAT5 and pSTAT1 were low (Figure 6F), stimulation with 4 U/mL Epo for 15 min strongly increased pSTAT5, without a significant induction of pSTAT1 (Figure 6G). Stimulation with 500 U/mL interferon alpha (IFNα), an established activator of STAT1 (Kisseleva et al., 2002), strongly induced pSTAT1 but also led to a considerable increase in pSTAT5 (Figure 6H). Co-stimulation with Epo and IFNα resulted in a strong increase in pSTAT5 and pSTAT1 (Figure 6I). In these experiments, we observed a strong positive correlation between pSTAT5 and pSTAT1 ($\rho = 0.89 \pm 0.02$). We further examined the correlation between pSTAT5 and pSTAT3. Again, pSTAT5 and pSTAT3 were low in unstimulated CFU-E cells (Figure 6J), whereas stimulation with 4 U/mL Epo for 15 min strongly increased pSTAT5 without significantly inducing pSTAT3 (Figure 6K). Although stimulation with 10 ng/mL interleukin (IL)-6 lead to the induction of pSTAT3 in other cell types (Schuringa et al., 2000), the effect on pSTAT3 in CFU-E cells was marginal but detectable (Figure 6L). CFU-E cells co-stimulated with Epo and IL-6 (Figure 6M) showed a positive correlation between pSTAT5 and pSTAT3 ($\rho = 0.75 \pm 0.01$). To conclude, these experiments provide evidence that the cellular geometry not only determines the activation of STAT5 but also determines that of other STAT family members; therefore, we establish that cell-to-cell variability of the cytoplasmic volumes of CFU-E cells is a determinant of the noise in cellular information processing.

Threshold of nuclear phosphorylated STAT5 determines cell survival

In each individual CFU-E cell, survival is ensured by the Epo-induced production of phosphorylated STAT5 that enters the

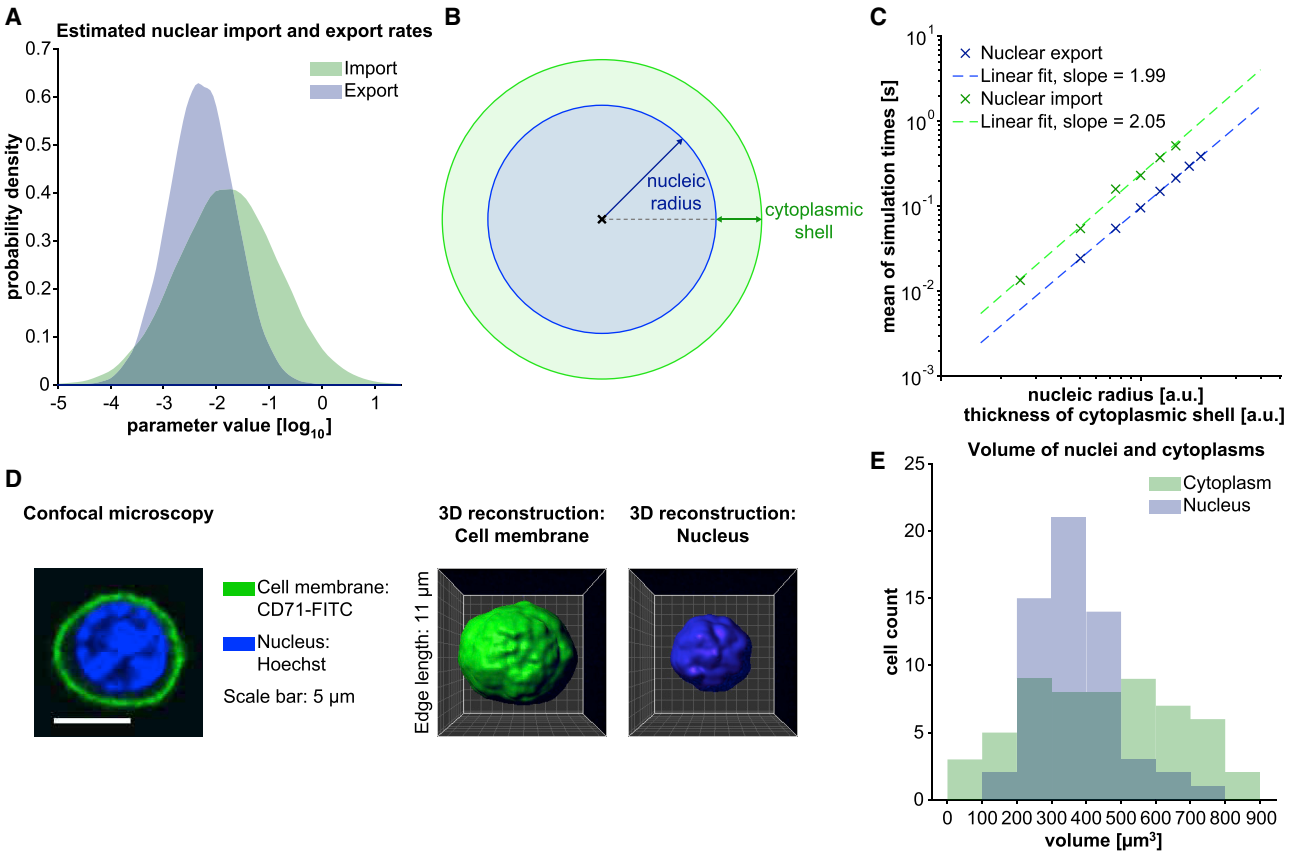

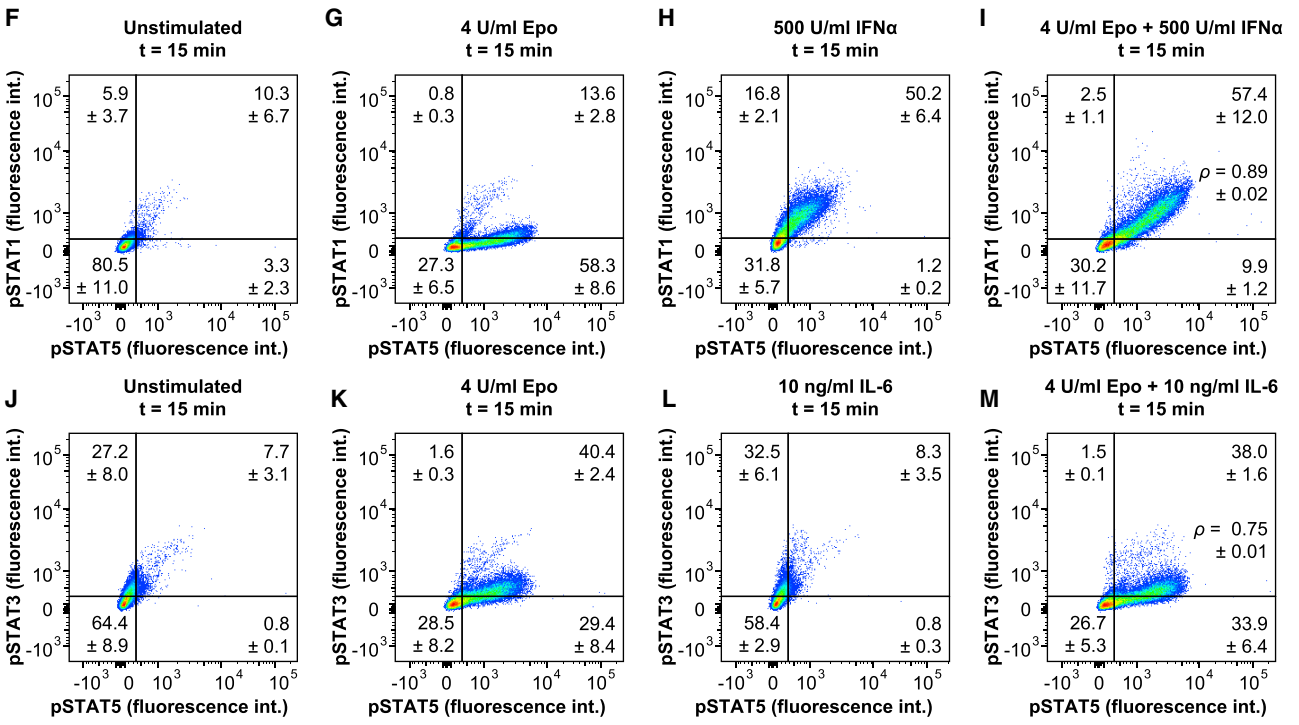

(legend on next page)

nucleus and induces sufficient amounts of anti-apoptotic gene products. However, it remained unresolved (1) whether the model-predicted cell-to-cell variability of nuclear pSTAT5 was sufficient to explain the experimentally observed survival data; (2) whether the cells had to acquire a certain amount of nuclear pSTAT5, corresponding to an absolute threshold; or (3) whether a certain fraction of the total STAT5 was required to be phosphorylated and in the nucleus, corresponding to a relative threshold. To address these questions, we established a link with the single-cell model between the abundance of nuclear pSTAT5 and the observed probability for CFU-E survival, depending on the Epo dose. We simulated nuclear pSTAT5 in each individual cell for different Epo concentrations and time windows between 30 and 180 min. The integrated, time-averaged abundance of nuclear pSTAT5 was compared with the fraction of surviving cells at the corresponding Epo concentrations. Based on model simulations (Figure S7A), we found that a relative threshold of nuclear pSTAT5 was significantly more informative than an absolute threshold to explain survival data of individual CFU-E cells. Further, these simulations indicated that the optimal time frame for integrating the abundance of nuclear pSTAT5 was the first 120 min after Epo stimulation, in line with the experimentally observed data of the fraction of surviving CFU-E upon stimulation with increasing Epo concentrations (Figure 7A). Additionally, the model simulations predicted that a surprisingly low fraction of about 0.29% of the total STAT5 had to be present as nuclear pSTAT5 to ensure the survival of an individual CFU-E cell (Figures 7B and S7B). This means that 24 to 118 nuclear pSTAT5 molecules are sufficient (i.e., 12–59 pSTAT5 dimers).

To determine which of the components of the JAK2/STAT5 signal transduction pathway with considerable cell-to-cell variability primarily determines the Epo-dependent life-or-death decision in individual CFU-E cells, the fraction of STAT5 in the nucleus versus the parameter values of those components in single cells was plotted, and surviving and apoptotic cells were indicated. Although the amount of the EpoR:JAK2 complex (Figure 7C) and SHP1 (Figure 7D) vary substantially in individual cells, only a weak, positive correlation of the EpoR:JAK2 complex and a weak, negative correlation of SHP1 with the fraction of STAT5 in the nucleus and, thus, survival were detected. The amount of total STAT5, although not having a large coefficient of variation, positively correlated with the fraction of nuclear STAT5 (Figure 7E), whereas the estimated offset of pSTAT5 in the cytoplasm was not correlated. Interestingly, a positive correlation with the fraction of nuclear STAT5 was predicted for the STAT5 import rate (Figure 7G), whereas the STAT5 export rate showed a weak, negative correlation with the fraction of STAT5 in the nucleus of individual CFU-E cells stimulated with Epo (Figure 7H).

Taken together, we confirmed that cell-to-cell variability in Epo-induced pSTAT5 was derived from several non-linear regulatory steps. A surprisingly low threshold amount of total STAT5 present as pSTAT5 in the nucleus of an individual CFU-E cell was sufficient to prevent apoptosis and to ensure survival of CFU-E cells upon stimulation with Epo. We demonstrated that the STAT5 import rate, which depends on the cytoplasmic volume, had the largest contribution to the fraction of STAT5 in the nucleus and, thus, to survival of individual CFU-E cells.

DISCUSSION

In this study, by combining population-level and single-cell data, we discovered multiple sources of cell-to-cell variability in Epo-induced JAK2/STAT5 signal transduction in CFU-E cells. The number of EpoR:JAK2 complexes, as well as the abundance of the phosphatase SHP1 and the cytoplasmic volume are responsible for the variability in pSTAT5 upon Epo stimulation. Of note, these three components or processes are membrane linked. In addition, we identified a relative threshold of 0.29% of total STAT5 being present as nuclear pSTAT5, which corresponds to as little as 24–118 molecules of nuclear pSTAT5 in a single CFU-E cell, required for survival.

We found that variability in the number of EpoR:JAK2 complexes contributed to the cell-to-cell variability in nuclear pSTAT5 in CFU-E cells. In line with our findings, it was shown that variability in the epidermal growth factor (EGF) receptor (EGFR) accounts for cell-to-cell variability in the amount of ERK in the nucleus of rat PC12 pheochromocytoma cells stimulated with EGF (Iwamoto et al., 2016).

The analysis of our mathematical model identified the hematopoietic tyrosine phosphatase SHP1 as another key component contributing to the observed variability in nuclear pSTAT5 in CFU-E cells upon Epo stimulation. The mathematical model

Figure 6. Model simulations of distributions of individual STAT5 import and export rates and experimental validation of the distribution of the nuclear-cytoplasmic translocation of STAT5 in CFU-E cells

(A) Estimated cell-to-cell variability of the import and export rate constants of STAT5 from the single-cell JAK2/STAT5 model.

(B) Schematic cross section of a cell indicating the important quantities for nuclear-cytoplasmic translocation rates.

(C) Results from simulated 10,000 random walks with fixed step size for different radii of the nucleic sphere core and thicknesses of cytoplasmic shells.

(D) The nucleus of unstimulated growth-factor-depleted CFU-E cells was stained with Hoechst, cells were fixed, and the cell membrane was labeled with FITC-coupled antibodies against CD71. Z stack images were acquired by confocal microscopy and used for 3D reconstructions of the cell membrane and the nucleus.

(E) Distributions of reconstructed cytoplasmic and nuclear volumes from CFU-E cells are shown (n = 58 cells). See Figures S6H and S6I for the volume of nucleus and cytoplasm in relation to the volume of the whole cell.

(F–I) Growth-factor-depleted CFU-E cells were fixed, permeabilized, intracellularly stained with anti-pSTAT5 antibodies coupled to Pacific Blue and anti-pSTAT1 antibodies coupled to Alexa Fluor 488 and analyzed by flow cytometry. Growth-factor-depleted CFU-E cells were (F) left unstimulated or were stimulated with (G) 4 U/mL Epo, (H) 500 U/mL IFNα, or (I) co-stimulated with 4 U/mL Epo and 500 U/mL IFNα for 15 min.

(J–M) Growth-factor-depleted CFU-E cells were fixed, permeabilized, and intracellularly stained with anti-pSTAT5 antibodies coupled to Pacific Blue and anti-pSTAT3 antibodies coupled to Alexa Fluor 488. Growth-factor-depleted CFU-E cells were (J) left unstimulated or were stimulated with (K) 4 U/mL Epo, (L) 10 ng/mL IL-6, or (I) co-stimulated with 4 U/mL Epo and 10 ng/mL IL-6. Experiments were performed in biological quadruplicates, and mean values with standard deviations are shown. Fluorescence intensities of a representative replicate are shown as pseudocolor density plots with bi-exponential axes.

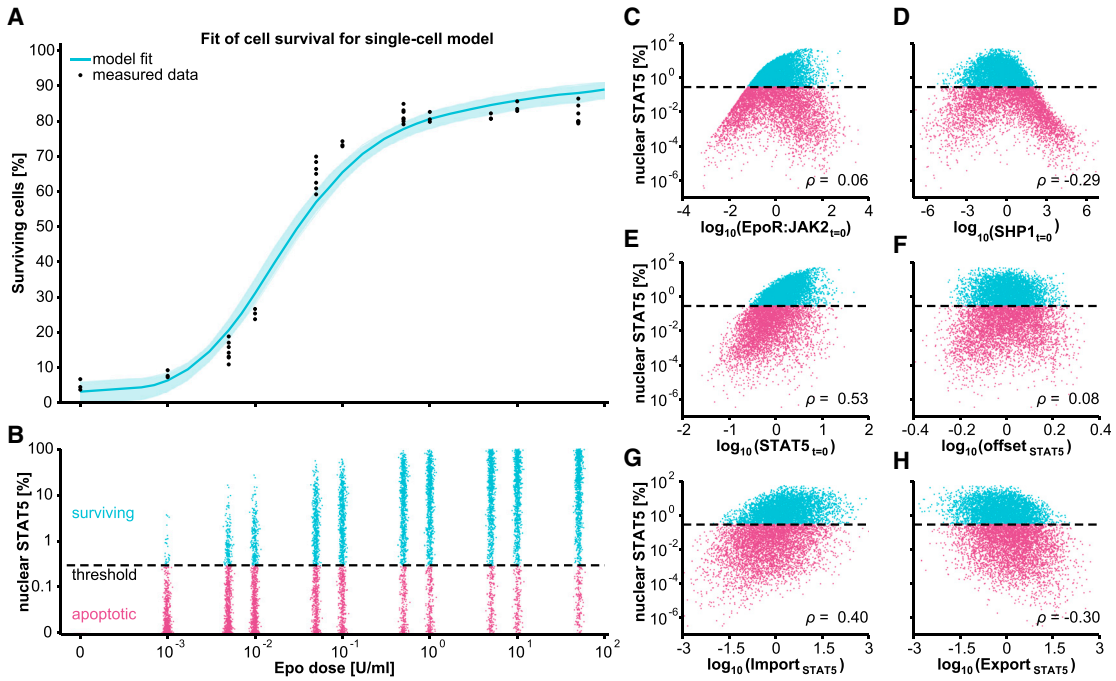

Figure 7. Calibration of the selected JAK2/STAT5 model for cell survival and the influence of random effects on the survival signal

(A and B) Single-cell model calibrated to experimental data of cell survival of CFU-E cells in response to stimulation with the indicated Epo dose. Based on the selected single-cell model, survival criteria based on an absolute or a relative amount of pSTAT5 in the nucleus were compared (see Figure S7). The fit of the survival model based on a relative threshold of 0.29% of total STAT5 during 120 min is depicted as a blue line; the light blue band indicates model uncertainty. (B) Simulated CFU-E cell populations of survival model based on a relative threshold of 0.29% of total STAT5 during 120 min, visualized for measured Epo doses. (C–H) Single-cell parameter values for a simulated cell population (Epo at half-effective concentration EC_{50} = 0.032 U/mL) plotted against the fraction of STAT5 in the nucleus. Dashed black line indicates threshold for cell survival.

predicted that the abundance of SHP1 showed the highest cell-to-cell variability among the analyzed cellular components. We experimentally validated this model prediction by flow cytometry experiments. To show that SHP1 levels dictate the levels of pSTAT5 and subsequent CFU-E survival, experimentally, it would be required to isolate cells prospectively with high versus low amounts of SHP1. However, such experiments require the analysis of living cells and thus are incompatible with intracellular staining of primary cells. Rather, we here observed these mechanisms by calibrating a mathematical model based on experimental data that were experimentally validated using independent datasets, including the detection of the cell-to-cell variability of SHP1 in erythroid progenitor cells by flow cytometry. Thus, we employed mathematics to answer an experimentally unobservable relationship, following the claim that "Mathematics is biology's next microscope, only better" (Cohen, 2004).

Furthermore, we found that the STAT5 import rate, which depends on the cytoplasmic volume, had the largest contribution to the heterogeneity in survival of individual CFU-E cells upon Epo stimulation. In general, nuclear-cytoplasmic translocation rates depend on compartment volumes as proposed by Chara and Brusch (2015). Here, we showed a tight coupling of STAT5 transport parameters with cytoplasmic and nucleoplasmic volumes. The large variability in the nuclear import rate of STAT5 in CFU-E cells identified with the model is explained by the large cell-to-cell variability of the cytoplasmic volume of CFU-E cells observed experimentally. This variability in volume might originate from two major sources: it was reported that CFU-E cells can *ex vivo* undergo up to four divisions within 27 h and, thus, exhibit a rather short cell-cycle duration (Nijhof et al., 1984), which might propagate volumetric fluctuations because of rapid successions of cell division. Further, during the differentiation of CFU-E cells to erythroblasts, the cell volume decreases gradually. The proposed interdependency between CFU-E cell-cycle progression and differentiation (Pop et al., 2010) could lead to a propagation of the variability that occurs in the cytoplasmic volumes during the G1 phase of the cell cycle, when CFU-E cells have to grow rapidly to reach a critical size for division and differentiation.

The larger variability observed in nuclear import of pSTAT5 compared with nuclear export of STAT5 could be explained by recently reported observations suggesting that binding of transcription factors to DNA can act as a passive noise filter and reduce the cell-to-cell variability in nuclear export processes (Battich et al., 2015; Stoeger et al., 2016). The comparison of Epo-induced JAK2/STAT5 signaling between mouse CFU-E cells and the human lung cancer cell line H838 by employing L_1 regularization to infer cell-type-specific parameters in the mathematical model predicted that one of the seven parameters differentially regulated between the cell types was the import rate of pSTAT5 to the nucleus (Merkle et al., 2016), underscoring the potential importance of nuclear import of pSTAT5 for the outcome of the response.

Here, we provided evidence that the cell-to-cell variability in cytoplasmic volumes affect the nuclear import rate not only of STAT5 but also of other STAT family members, such as STAT1 and STAT3, leading to a high correlation of pSTAT1 and pSTAT3 to pSTAT5. In erythroid cells prepared from the spleens of mice infected with the anemia-inducing strain of Friend virus (Penta and Sawyer, 1995) and in the Epo-hypersensitive acute megakaryoblastic leukemia cell line UT-7/Epo (Kirito et al., 1997), it was previously reported that Epo can induce pSTAT1 and pSTAT3. However, in CFU-E cells isolated from fetal mouse livers, Epo failed to activate STAT1, whereas IFNα treatment resulted in a strong increase in pSTAT1. Further, pSTAT3 in CFU-E cells was not induced by Epo but was only induced in response to treatment with IL-6. Although it is established that IL-3 and IL-6 act synergistically to support proliferation of different Epo-dependent murine progenitor cells (Ikebuchi et al., 1987), time-resolved experiments in BFU-E cells—the predecessors of CFU-E cells—revealed a more complicated pattern: addition of IL-6 added on day 0 had a stimulatory effect on proliferation, whereas IL-6 added on day 7 had an inhibitory effect on BFU-E colony growth (Ferry et al., 1997). These and our results support the importance of ligand- and organ-specific differences in STAT1 and STAT3 activation in the erythroid lineage.

The observed strong correlation between pSTAT5 and pSTAT1 or pSTAT3, respectively, could potentially be explained by three mechanisms: first, it could be that all three STAT family members were activated by Epo, as reported previously for other cell types. However, our results demonstrated that, in erythroid progenitor cells at the CFU-E stage isolated from fetal mouse livers, Epo only induces pSTAT5. Second, it was previously shown that the levels of proteins in the same biological pathway were far more correlated than those of proteins in different pathways (Sigal et al., 2006). This explanation can be ruled out because the IFNα-induced STAT1 and the IL-6-induced STAT3 signal transduction pathways employ different molecules than the Epo-induced JAK2/STAT5 pathway use: IFNα activates STAT1 via IFNAR1/2 and TYK2/JAK1 and IL-6 leads to phosphorylation of STAT3 via IL6RA/GP130 and JAK1 (Kisseleva et al., 2002). Third, the specific cell geometry in a given cell may be causative for the observed correlations because it is a factor shared by the STAT family members. As our model-based studies established the importance of the variability in the cytoplasmic volume for the heterogeneity of STAT5 phosphorylation, we propose the cytoplasmic volume as the determinant contributing to cell-to-cell variability in the activation of STAT family members.

Analysis of the transfer of information in biochemical networks by entropy-based methods pointed to the particular importance of noise (Cheong et al., 2011; Shockley et al., 2019; Suderman et al., 2017). In particular, Suderman et al. (2017) investigated information transfer at the single-cell and the cell-population level. They observed that for phenotypic responses (cell fate decisions), such as mating in yeast, which depend on accurate execution in single cells, the underlying signal transduction network operates highly reliably. In contrast, if the response in a percentage of cells in a cell population matters, surprisingly, variability at the single-cell level ensures a graded response of the cell population and increases information transfer at the cell-population level. Our study of Epo-induced survival of CFU-E cells supports that concept and is a practical example of the latter condition.

In conclusion, we present a two-step mathematical modeling strategy to integrate population-average data and single-cell data to determine a threshold for binary cell-fate decisions. This approach is scalable and can readily be applied to other cell-fate decisions, such as proliferation, migration, and differentiation, which are controlled by multiple transcription factors in health and disease.

STAR★METHODS

Detailed methods are provided in the online version of this paper and include the following:

- KEY RESOURCES TABLE
- RESOURCE AVAILABILITY
  - Lead contact
  - Materials availability
  - Data and code availability
- EXPERIMENTAL MODEL AND SUBJECT DETAILS
  - Preparation and stimulation of erythroid progenitor cells
  - Confocal microscopy and data analysis
  - Flow cytometry
  - Cell fractionation
  - Quantitative immunoblotting, qPCR and mass spectrometry
- METHOD DETAILS
  - Mathematical modeling of population-average data
  - Model topology and data integration
  - Parameter estimation and profile likelihood
  - Model reduction
  - Model equations
  - Mixed-effect modeling for cell population
  - Approximations to simulate cell populations
  - Monte Carlo sampling
  - Sigma point methods
  - Dirac mixture models
  - Parametrizations of covariance matrices
  - Parameter estimation for the single-cell models
- QUANTIFICATION AND STATISTICAL ANALYSIS
  - Model selection criteria
  - Translocation rates and compartmental volumes
  - Inference of the survival criterion

SUPPLEMENTAL INFORMATION

Supplemental information can be found online at https://doi.org/10.1016/j.celrep.2021.109507.

ACKNOWLEDGMENTS

We would like to thank the flow cytometry core facility of the DKFZ for support and Susen Lippmann for excellent technical assistance. We are grateful to Grégoire Altan-Bonnet (National Cancer Institute) for the kind gift of SHP1 and STAT5 antibodies and to Marieke Essers (DKFZ/HI-STEM) for providing murine IFNα. C.T. and J.T. acknowledge support by the state of Baden-Württemberg, Germany, through bwHPC, and the Deutsche

Forschungsgemeinschaft (DFG) through grant INST35/1134-1 FUGG. P.S. and J.H. acknowledge support by the European Union's Horizon 2020 research and innovation program (CanPathPro; grant no. 686282). L.A., C.T., J.H., U.K., and M.S. acknowledge funding by the German Ministry of Education and Research (BMBF) within the e:Bio collaborative research projects "Systems Biology of Erythropoietin" (SBEpo, 0316182A and 0316182B). J.T., M.S., and U.K. were supported by the German Federal Ministry of Education and Research (BMBF)-funded ERAPerMed consortium "Improved Treatments of Acute Myeloid Leukaemias by Personalised Medicine" (AML_PM, 01KU1902A and 01KU1902B). J.T. and U.K. were supported by the German Federal Ministry of Education and Research (BMBF)-funded e:Bio consortium MS_DILI (research grants 031L0074B and 031L0074A) and the Systems Medicine network LiSyM (research grants 031L0048 and 031L0042). C.T and J.T. were supported by the Deutsche Forschungsgemeinschaft (DFG) under Germany's Excellence Strategy—EXC-2189—project ID: 390939984. ORCID IDs—L.A.: 0000-0002-0971-2309; P.S.: 0000-0002-7567-3985; C.T.: 0000-0003-2822-5191; L.S.: 0000-0001-7946-3232; L.E.S.: 0000-0002-7151-9913; D.W.: 0000-0002-3277-5033; J.T.: 0000-0003-4517-1383; U.K.: 0000-0001-9845-3099; J.H.: 0000-0002-4935-3312; M.S.: 0000-0002-9517-5166.

AUTHOR CONTRIBUTION

M.S., J.H., U.K., and J.T. designed the study. L.A., L.E.S., and L.P. conducted the experiments. L.A. and L.E.S. analyzed the experimental data. C.T. and J.T. implemented, calibrated, and reduced the complexity of the ordinary differential equation (ODE) model of the population-average data. P.S. carried out the model selection for the single-cell models and developed and implemented the parameterization method for the covariance matrices. P.S., L.S., and J.H. implemented and calibrated the single-cell model. P.S., D.W., and J.H. implemented the Dirac mixture distribution. L.A., C.T., P.S., L.S., J.H., U.K., and M.S. wrote the manuscript, with input from J.T. All authors read and approved the manuscript.

DECLARATION OF INTERESTS

The authors declare no competing interests.

Received: December 6, 2020
Revised: April 1, 2021
Accepted: July 19, 2021
Published: August 10, 2021

REFERENCES

Adlung, L., Kar, S., Wagner, M.C., She, B., Chakraborty, S., Bao, J., Lattermann, S., Boerries, M., Busch, H., Wuchter, P., et al. (2017). Protein abundance of AKT and ERK pathway components governs cell type-specific regulation of proliferation. Mol. Syst. Biol. *13*, 904.

Bachmann, J., Raue, A., Schilling, M., Böhm, M.E., Kreutz, C., Kaschek, D., Busch, H., Gretz, N., Lehmann, W.D., Timmer, J., and Klingmüller, U. (2011). Division of labor by dual feedback regulators controls JAK2/STAT5 signaling over broad ligand range. Mol. Syst. Biol. *7*, 516.

Balsa-Canto, E., and Banga, J.R. (2011). AMIGO, a toolbox for advanced model identification in systems biology using global optimization. Bioinformatics *27*, 2311–2313.

Battich, N., Stoeger, T., and Pelkmans, L. (2015). Control of transcript variability in single mammalian cells. Cell *163*, 1596–1610.

Becker, V., Schilling, M., Bachmann, J., Baumann, U., Raue, A., Maiwald, T., Timmer, J., and Klingmüller, U. (2010). Covering a broad dynamic range: information processing at the erythropoietin receptor. Science *328*, 1404–1408.

Bodenmiller, B., Zunder, E.R., Finck, R., Chen, T.J., Savig, E.S., Bruggner, R.V., Simonds, E.F., Bendall, S.C., Sachs, K., Krutzik, P.O., and Nolan, G.P. (2012). Multiplexed mass cytometry profiling of cellular states perturbed by small-molecule regulators. Nat. Biotechnol. *30*, 858–867.

Boehm, M.E., Adlung, L., Schilling, M., Roth, S., Klingmüller, U., and Lehmann, W.D. (2014). Identification of isoform-specific dynamics in phosphorylation-dependent STAT5 dimerization by quantitative mass spectrometry and mathematical modeling. J. Proteome Res. *13*, 5685–5694.

Bressloff, P.C. (2014). Stochastic Processes in Cell Biology (Springer).

Buettner, F., Natarajan, K.N., Casale, F.P., Proserpio, V., Scialdone, A., Theis, F.J., Teichmann, S.A., Marioni, J.C., and Stegle, O. (2015). Computational analysis of cell-to-cell heterogeneity in single-cell RNA-sequencing data reveals hidden subpopulations of cells. Nat. Biotechnol. *33*, 155–160.

Chara, O., and Brusch, L. (2015). Mathematical modelling of fluid transport and its regulation at multiple scales. Biosystems *130*, 1–10.

Cheong, R., Rhee, A., Wang, C.J., Nemenman, I., and Levchenko, A. (2011). Information transduction capacity of noisy biochemical signaling networks. Science *334*, 354–358.

Cohen, J.E. (2004). Mathematics is biology's next microscope, only better; biology is mathematics' next physics, only better. PLoS Biol. *2*, e439.

Dalerba, P., Kalisky, T., Sahoo, D., Rajendran, P.S., Rothenberg, M.E., Leyrat, A.A., Sim, S., Okamoto, J., Johnston, D.M., Qian, D., et al. (2011). Single-cell dissection of transcriptional heterogeneity in human colon tumors. Nat. Biotechnol. *29*, 1120–1127.

Ellis, B., Haaland, P., Hahne, F., Le Meur, N., Gopalakrishnan, N., Spidlen, J., and Jiang, M. (2018). flowCore: basic structures for flow cytometry data (R package version 1.48.0. (Bioconductor)). https://doi.org/10.18129/B9.bioc.flowCore. http://bioconductor.statistik.tu-dortmund.de/packages/3.6/bioc/html/flowCore.html.

Ferry, A.E., Baliga, S.B., Monteiro, C., and Pace, B.S. (1997). Globin gene silencing in primary erythroid cultures. An inhibitory role for interleukin-6. J. Biol. Chem. *272*, 20030–20037.

Fröhlich, F., Theis, F.J., Rädler, J.O., and Hasenauer, J. (2017). Parameter estimation for dynamical systems with discrete events and logical operations. Bioinformatics *33*, 1049–1056.

Fröhlich, F., Reiser, A., Fink, L., Woschée, D., Ligon, T., Theis, F.J., Rädler, J.O., and Hasenauer, J. (2018). Multi-experiment nonlinear mixed effect modeling of single-cell translation kinetics after transfection. NPJ Syst. Biol. Appl. *5*, 1.

Gilitschenski, I., and Hanebeck, U.D. (2013). Efficient deterministic dirac mixture approximation of Gaussian distributions. In American Control Conference (ACC'13), L. Pao, ed. (IEEE), pp. 2422–2427.

Gillespie, D.T. (1977). Exact stochastic simulation of coupled chemical reactions. J. Phys. Chem. *81*, 2340–2361.

Gobert, S., Chretien, S., Gouilleux, F., Muller, O., Pallard, C., Dusanter-Fourt, I., Groner, B., Lacombe, C., Gisselbrecht, S., and Mayeux, P. (1996). Identification of tyrosine residues within the intracellular domain of the erythropoietin receptor crucial for STAT5 activation. EMBO J. *15*, 2434–2441.

Gouilleux, F., Pallard, C., Dusanter-Fourt, I., Wakao, H., Haldosen, L.A., Norstedt, G., Levy, D., and Groner, B. (1995). Prolactin, growth hormone, erythropoietin and granulocyte-macrophage colony stimulating factor induce MGF-Stat5 DNA binding activity. EMBO J. *14*, 2005–2013.

Hahn, B., D'Alessandro, L.A., Depner, S., Waldow, K., Boehm, M.E., Bachmann, J., Schilling, M., Klingmüller, U., and Lehmann, W.D. (2013). Cellular ERK phospho-form profiles with conserved preference for a switch-like pattern. J. Proteome Res. *12*, 637–646.

Hanebeck, U.D., and Klumpp, V. (2008). Localized cumulative distributions and a multivariate generalization of the Cramér-von Mises distance. In Proceedings of the 2008 IEEE International Conference on Multisensor Fusion and Integration for Intelligent Systems, L. Suk-han, H. Ko, and H. Hahn, eds. (IEEE), pp. 33–39.

Hass, H., Kipkeew, F., Gauhar, A., Bouché, E., May, P., Timmer, J., and Bock, H.H. (2017). Mathematical model of early Reelin-induced Src family kinase-mediated signaling. PLoS ONE *12*, e0186927.

Heinrich, A.C., Pelanda, R., and Klingmüller, U. (2004). A mouse model for visualization and conditional mutations in the erythroid lineage. Blood *104*, 659–666.

Herzenberg, L.A., Tung, J., Moore, W.A., Herzenberg, L.A., and Parks, D.R. (2006). Interpreting flow cytometry data: a guide for the perplexed. Nat. Immunol. *7*, 681–685.

Hindmarsh, A.C., Brown, P.N., Grant, K.E., Lee, S.L., Serban, R., Shumaker, D.E., and Woodward, C.S. (2005). SUNDIALS: suite of nonlinear and differential/algebraic equation solvers. ACM Trans. Math. Softw. *31*, 363–396.

Hoops, S., Sahle, S., Gauges, R., Lee, C., Pahle, J., Simus, N., Singhal, M., Xu, L., Mendes, P., and Kummer, U. (2006). COPASI—a complex pathway simulator. Bioinformatics *22*, 3067–3074.

Ikebuchi, K., Wong, G.G., Clark, S.C., Ihle, J.N., Hirai, Y., and Ogawa, M. (1987). Interleukin 6 enhancement of interleukin 3-dependent proliferation of multipotential hemopoietic progenitors. Proc. Natl. Acad. Sci. USA *84*, 9035–9039.

Iwamoto, K., Shindo, Y., and Takahashi, K. (2016). Modeling cellular noise underlying heterogeneous cell responses in the epidermal growth factor signaling pathway. PLoS Comput. Biol. *12*, e1005222.

Karlsson, M., Janzén, D.L., Durrieu, L., Colman-Lerner, A., Kjellsson, M.C., and Cedersund, G. (2015). Nonlinear mixed-effects modelling for single cell estimation: when, why, and how to use it. BMC Syst. Biol. *9*, 52.

Kirito, K., Uchida, M., Yamada, M., Miura, Y., and Komatsu, N. (1997). A distinct function of STAT proteins in erythropoietin signal transduction. J. Biol. Chem. *272*, 16507–16513.

Kisseleva, T., Bhattacharya, S., Braunstein, J., and Schindler, C.W. (2002). Signaling through the JAK/STAT pathway, recent advances and future challenges. Gene *285*, 1–24.

Klingmüller, U., Bergelson, S., Hsiao, J.G., and Lodish, H.F. (1996). Multiple tyrosine residues in the cytosolic domain of the erythropoietin receptor promote activation of STAT5. Proc. Natl. Acad. Sci. USA *93*, 8324–8328.

Koulnis, M., Porpiglia, E., Hidalgo, D., and Socolovsky, M. (2014). Erythropoiesis: from molecular pathways to system properties. Adv. Exp. Med. Biol. *844*, 37–58.

Le Novère, N., Hucka, M., Mi, H., Moodie, S., Schreiber, F., Sorokin, A., Demir, E., Wegner, K., Aladjem, M.I., Wimalaratne, S.M., et al. (2009). The systems biology graphical notation. Nat. Biotechnol. *27*, 735–741.

Loos, C., Moeller, K., Fröhlich, F., Hucho, T., and Hasenauer, J. (2018). A hierarchical, data-driven approach to modeling single-cell populations predicts latent causes of cell-to-cell variability. Cell Syst. *6*, 593–603.e13.

MacDonald, N. (1976). Time delay in simple chemostat models. Biotechnol. Bioeng. *18*, 805–812.

Maiwald, T., Hass, H., Steiert, B., Vanlier, J., Engesser, R., Raue, A., Kipkeew, F., Bock, H.H., Kaschek, D., Kreutz, C., and Timmer, J. (2016). Driving the model to its limit: profile likelihood based model reduction. PLoS ONE *11*, e0162366.

Merkle, R., Steiert, B., Salopiata, F., Depner, S., Raue, A., Iwamoto, N., Schelker, M., Hass, H., Wäsch, M., Böhm, M.E., et al. (2016). Identification of cell type-specific differences in erythropoietin receptor signaling in primary erythroid and lung cancer cells. PLoS Comput. Biol. *12*, e1005049.

Moore, W.A., and Parks, D.R. (2012). Update for the logicle data scale including operational code implementations. Cytometry A *81*, 273–277.

Neel, B.G., Gu, H., and Pao, L. (2003). The 'Shp'ing news: SH2 domain-containing tyrosine phosphatases in cell signaling. Trends Biochem. Sci. *28*, 284–293.

Neuert, G., Munsky, B., Tan, R.Z., Teytelman, L., Khammash, M., and van Oudenaarden, A. (2013). Systematic identification of signal-activated stochastic gene regulation. Science *339*, 584–587.

Niepel, M., Spencer, S.L., and Sorger, P.K. (2009). Non-genetic cell-to-cell variability and the consequences for pharmacology. Curr. Opin. Chem. Biol. *13*, 556–561.

Nijhof, W., and Wierenga, P.K. (1983). Isolation and characterization of the erythroid progenitor cell: CFU-E. J. Cell Biol. *96*, 386–392.

Nijhof, W., Wierenga, P.K., Pietens, J., and Bloem, R. (1984). Cell kinetic behaviour of a synchronized population of erythroid precursor cells in vitro. Cell Tissue Kinet. *17*, 629–639.

Parks, D.R., Roederer, M., and Moore, W.A. (2006). A new "logicle" display method avoids deceptive effects of logarithmic scaling for low signals and compensated data. Cytometry A *69*, 541–551.

Paszek, P., Ryan, S., Ashall, L., Sillitoe, K., Harper, C.V., Spiller, D.G., Rand, D.A., and White, M.R. (2010). Population robustness arising from cellular heterogeneity. Proc. Natl. Acad. Sci. USA *107*, 11644–11649.

Pelkmans, L. (2012). Cell biology: using cell-to-cell variability—a new era in molecular biology. Science *336*, 425–426.

Penta, K., and Sawyer, S.T. (1995). Erythropoietin induces the tyrosine phosphorylation, nuclear translocation, and DNA binding of STAT1 and STAT5 in erythroid cells. J. Biol. Chem. *270*, 31282–31287.

Perfetto, S.P., Chattopadhyay, P.K., and Roederer, M. (2004). Seventeen-colour flow cytometry: unravelling the immune system. Nat. Rev. Immunol. *4*, 648–655.

Pinheiro, J.C., and Bates, D.M. (1996). Unconstrained parametrizations for variance-covariance matrices. Stat. Comput. *6*, 289–296.

Pop, R., Shearstone, J.R., Shen, Q., Liu, Y., Hallstrom, K., Koulnis, M., Gribnau, J., and Socolovsky, M. (2010). A key commitment step in erythropoiesis is synchronized with the cell cycle clock through mutual inhibition between PU.1 and S-phase progression. PLoS Biol. *8*, e1000484.

Potter, M. (1985). History of the BALB/c family. Curr. Top. Microbiol. Immunol. *122*, 1–5.

Raj, A., and van Oudenaarden, A. (2008). Nature, nurture, or chance: stochastic gene expression and its consequences. Cell *135*, 216–226.

Raue, A., Kreutz, C., Maiwald, T., Bachmann, J., Schilling, M., Klingmüller, U., and Timmer, J. (2009). Structural and practical identifiability analysis of partially observed dynamical models by exploiting the profile likelihood. Bioinformatics *25*, 1923–1929.

Raue, A., Becker, V., Klingmüller, U., and Timmer, J. (2010). Identifiability and observability analysis for experimental design in nonlinear dynamical models. Chaos *20*, 045105.

Raue, A., Kreutz, C., Theis, F.J., and Timmer, J. (2012a). Joining forces of Bayesian and frequentist methodology: a study for inference in the presence of non-identifiability. Philos. Trans.- Royal Soc., Math. Phys. Eng. Sci. *371*, 20110544.

Raue, A., Schilling, M., Bachmann, J., Matteson, A., Schelker, M., Kaschek, D., Hug, S., Kreutz, C., Harms, B.D., Theis, F.J., et al. (2013b). Lessons learned from quantitative dynamical modeling in systems biology. PLoS ONE *8*, e74335.

Raue, A., Steiert, B., Schelker, M., Kreutz, C., Maiwald, T., Hass, H., Vanlier, J., Tönsing, C., Adlung, L., Engesser, R., et al. (2015). Data2Dynamics: a modeling environment tailored to parameter estimation in dynamical systems. Bioinformatics *31*, 3558–3560.

Sasaki, A., Yasukawa, H., Shouda, T., Kitamura, T., Dikic, I., and Yoshimura, A. (2000). CIS3/SOCS-3 suppresses erythropoietin (EPO) signaling by binding the EPO receptor and JAK2. J. Biol. Chem. *275*, 29338–29347.

Schuringa, J.J., Wierenga, A.T., Kruijer, W., and Vellenga, E. (2000). Constitutive Stat3, Tyr705, and Ser727 phosphorylation in acute myeloid leukemia cells caused by the autocrine secretion of interleukin-6. Blood *95*, 3765–3770.

Schwanhäusser, B., Busse, D., Li, N., Dittmar, G., Schuchhardt, J., Wolf, J., Chen, W., and Selbach, M. (2011). Global quantification of mammalian gene expression control. Nature *473*, 337–342.

Schwarz, G. (1978). Estimating the dimension of a model. Ann. Stat. *6*, 461–464.

Shockley, E.M., Rouzer, C.A., Marnett, L.J., Deeds, E.J., and Lopez, C.F. (2019). Signal integration and information transfer in an allosterically regulated network. NPJ Syst. Biol. Appl. *5*, 23.

Sigal, A., Milo, R., Cohen, A., Geva-Zatorsky, N., Klein, Y., Liron, Y., Rosenfeld, N., Danon, T., Perzov, N., and Alon, U. (2006). Variability and memory of protein levels in human cells. Nature *444*, 643–646.

Simpson, M.J., Baker, R.E., Vittadello, S.T., and Maclaren, O.J. (2020). Practical parameter identifiability for spatio-temporal models of cell invasion. J. R. Soc. Interface *17*, 20200055.

Socolovsky, M., Fallon, A.E., Wang, S., Brugnara, C., and Lodish, H.F. (1999). Fetal anemia and apoptosis of red cell progenitors in Stat5a$^{-/-}$5b$^{-/-}$ mice: a direct role for Stat5 in Bcl-X(L) induction. Cell *98*, 181–191.

Socolovsky, M., Nam, H., Fleming, M.D., Haase, V.H., Brugnara, C., and Lodish, H.F. (2001). Ineffective erythropoiesis in Stat5a$^{-/-}$5b$^{-/-}$ mice due to decreased survival of early erythroblasts. Blood *98*, 3261–3273.

Stapor, P., Weindl, D., Ballnus, B., Hug, S., Loos, C., Fiedler, A., Krause, S., Hroß, S., Fröhlich, F., and Hasenauer, J. (2018). PESTO: parameter estimation toolbox. Bioinformatics *34*, 705–707.

Stoeger, T., Battich, N., and Pelkmans, L. (2016). Passive noise filtering by cellular compartmentalization. Cell *164*, 1151–1161.

Suderman, R., Bachman, J.A., Smith, A., Sorger, P.K., and Deeds, E.J. (2017). Fundamental trade-offs between information flow in single cells and cellular populations. Proc. Natl. Acad. Sci. USA *114*, 5755–5760.

Swameye, I., Müller, T.G., Timmer, J., Sandra, O., and Klingmüller, U. (2003). Identification of nucleocytoplasmic cycling as a remote sensor in cellular signaling by databased modeling. Proc. Natl. Acad. Sci. USA *100*, 1028–1033.

Taniguchi, Y., Choi, P.J., Li, G.W., Chen, H., Babu, M., Hearn, J., Emili, A., and Xie, X.S. (2010). Quantifying E. coli proteome and transcriptome with single-molecule sensitivity in single cells. Science *329*, 533–538.

Toni, T., and Tidor, B. (2013). Combined model of intrinsic and extrinsic variability for computational network design with application to synthetic biology. PLoS Comput. Biol. *9*, e1002960.

Tönsing, C., Timmer, J., and Kreutz, C. (2018). Profile likelihood-based analyses of infectious disease models. Stat. Methods Med. Res. *27*, 1979–1998.

van der Merwe, R. (2004). Sigma-point Kalman filters for probabilistic inference in dynamic state-space models (Oregon Health and Science University), PhD dissertation.

Weill, U., Krieger, G., Avihou, Z., Milo, R., Schuldiner, M., and Davidi, D. (2019). Assessment of GFP Tag Position on Protein Localization and Growth Fitness in Yeast. J. Mol. Biol. *431*, 636–641.

Yoshimura, A., Ohkubo, T., Kiguchi, T., Jenkins, N.A., Gilbert, D.J., Copeland, N.G., Hara, T., and Miyajima, A. (1995). A novel cytokine-inducible gene CIS encodes an SH2-containing protein that binds to tyrosine-phosphorylated interleukin 3 and erythropoietin receptors. EMBO J. *14*, 2816–2826.

Zechner, C., Ruess, J., Krenn, P., Pelet, S., Peter, M., Lygeros, J., and Koeppl, H. (2012). Moment-based inference predicts bimodality in transient gene expression. Proc. Natl. Acad. Sci. USA *109*, 8340–8345.

STAR★METHODS

KEY RESOURCES TABLE

REAGENT or RESOURCE	SOURCE	IDENTIFIER
Antibodies		
Anti-mouse Stat5 (polyclonal (C-17)-G)	Santa Cruz	sc-835-G; RRID:AB_632447
Anti-mouse Phospho-STAT5 (monoclonal C11C5)	Cell Signaling	Cat# 9359; RRID:AB_823649
Anti-SHP1 (SH-PTP1, polyclonal (C-19))	Santa Cruz	sc-287; RRID:AB_2173829
Donkey anti-rabbit IgG (H+L)-APC (polyclonal)	Jackson ImmunoResearch	Cat# 711-136-152; RRID:AB_2340601
Donkey anti-goat IgG (H+L)-FITC (polyclonal)	Jackson ImmunoResearch	Cat# 705-095-147; RRID:AB_2340401
Rat anti-mouse CD71-FITC (monoclonal RI7217)	BioLegend	Cat# 113805; RRID:AB_313566
BD Phosflow Pacific Blue mouse anti-STAT5 (pY694)	BD Biosciences	Cat# 560311; RRID:AB_1645497
BD Phosflow Alexa Fluor 488 mouse anti-STAT1 (pY701)	BD Biosciences	Cat# 612596; RRID:AB_399879
BD Phosflow Alexa Fluor 488 mouse anti-STAT3 (pY705)	BD Biosciences	Cat# 557814; , RRID:AB_647098
Chemicals, peptides, and recombinant proteins		
Erythropoietin (Erypo FS 10000)	Janssen	PZN: 6301292
IFNα (recombinant mouse interferon α)	Milytenyi Biotec	Cat# 130-093-131
IL-6 (recombinant murine Interleukin-6)	PeproTech	Cat# 216-16
Red Blood Cell Lysing Buffer Hybri-Max	Sigma	Cat# R7757
Hoechst	Santa Cruz	sc-396575
Polyvinyl alcohol mounting medium with DABCO	Sigma Aldrich	Cat# M1289
Critical commercial assays		
EasySep Mouse Hematopoietic Progenitor Cell Isolation Kit	StemCell Technologies	Cat # 19856
Deposited data		
Raw and analyzed data	This paper	https://zenodo.org/record/5091784
Experimental models: Cell lines		
BaF3	DSMZ	RRID:CVCL_0161
Experimental models: Organisms/strains		
BALB/c	Envigo	BALB/cOlaHsd; Order code 162
Recombinant DNA		
pMOWS-SHP1	(Bachmann et al., 2011)	N/A
Software and algorithms		
MATLAB (including the Optimization Toolbox, the Statistics Toolbox and the Symbolic Toolbox), version R2016a and R2017a	The Mathworks	https://www.mathworks.com
Advanced Multilanguage Interface for CVODES and IDAS (AMICI)	(Fröhlich et al., 2017)	https://github.com/AMICI-dev/AMICI
Parameter Estimation Toolbox (PESTO)	(Stapor et al., 2018)	Parameter Estimation Toolbox (PESTO)
MATLAB toolbox for Mixed Effect Model InfeRence (MEMOIR)	(Fröhlich et al., 2018)	https://github.com/ICB-DCM/MEMOIR
Data2Dynamics (D2D)	(Raue et al., 2015)	https://github.com/Data2Dynamics/d2d
FlowJo V.10.0.8	FlowJo, LLC	https://www.flowjo.com/
Imaris software, version 7.7.2	Bitplane	https://imaris.oxinst.com/packages
MATLAB implementation of FlowCore	(Ellis et al., 2018)	https://github.com/nolanlab/MatlabCytofUtilities/tree/master/logicle

RESOURCE AVAILABILITY

Lead contact

Further information and requests for resources and reagents should be directed to and will be fulfilled by the lead contact, Marcel Schilling (M.Schilling@dkfz.de).

Materials availability

This study did not generate new unique reagents.

Data and code availability

The experimental data and the implementation of the models and parameter estimation tools used in this study are available on Zenodo: https://zenodo.org/record/5091784. The code for population-average and single-cell models is maintained on GitHub: https://github.com/Data2Dynamics/d2d, https://github.com/ICB-DCM/MEMOIR.

EXPERIMENTAL MODEL AND SUBJECT DETAILS

Preparation and stimulation of erythroid progenitor cells

All mice of this work were housed at the DKFZ animal facility under constant light/dark cycles. Animals were maintained on a standard mouse diet and allowed *ad libitum* access to food and water. All animal experiments were approved by the governmental review committee on animal care of the federal state of Baden-Württemberg, Germany (reference number DKFZ215).

Fetal mouse livers at embryonic day 13.5 (i.e., during massive erythroid expansion) were isolated from the uteri of sacrificed BALB/c mice (Potter, 1985). Fetal liver cells (FLCs) were resuspended in 500 μl of 0.3% BSA/PBS, flushed through a 40 μm cell strainer (BD Biosciences) and taken up in 10 mL Red Blood Cell Lysing Buffer (Sigma-Aldrich). The suspension of 40 fetal livers was subjected to negative depletion by using magnetic beads (Miltenyi Biotech). Freshly purified CFU-E cells were cultivated for 14 h in Panserin 401 (PAN-Biotech) supplemented with 50 μM 2-mercaptoethanol and 0.5 U/ml Epo. Subsequently, CFU-E cells were washed three times with Panserin 401 supplemented with 50 μM 2-mercaptoethanol and deprived from growth factors in Panserin 401 supplemented with 50 μM 2-mercaptoethanol and 1 mg/ml BSA at 37°C for 1 h. Stimulations with Epo, IFNα or IL-6 were performed with 2×10^6 cells in 250 μl Panserin 401 in a thermomixer at 37°C, shaking at 800 rpm.

Confocal microscopy and data analysis

Staining of the nucleus was performed with 2 μg/ml Hoechst (Santa Cruz, Catalog #sc-396575) at a cell density of 10×10^6 cells/ml for 20 min at 37°C, shaking at 800 rpm. The cells were fixated in 4% formaldehyde, followed by staining of the plasma membrane with 15 μg/ml FITC-coupled rat anti-mouse CD71 (Biolegend, Cat# 113805) for 30 min at room temperature. For microscopy the cells were mixed 1:1 with Polyvinyl alcohol mounting medium with DABCO (Sigma Aldrich, Cat# M1289).

Confocal microscopy was performed with the ZEISS LSM 710 ConfoCor 3 using a 43x magnification oil objective. FITC and Hoechst (Santa Cruz, Catalog #sc-396575) were excited by a 488 nm and 405 nm Argon Laser, respectively. Z stacks with an interval of 0.5 μm were taken and subsequently three-dimensionally reconstructed with the ImageJ software (version 1.4.3.67). The nuclear and cytoplasmic volumes were calculated by artificially filling the volume enclosed by the stain using the Fill Holes and 3D Objects Counter commands. For illustrative purposes, the cells were three-dimensionally reconstructed with the Imaris software (version 7.7.2) and the shape of the plasma membrane and the nucleus were highlighted with the Surface function.

Flow cytometry

Cultivation of parental BaF3 cells and retroviral transduction of BaF3 cells with pMOWS-SHP1 (Bachmann et al., 2011) was performed as previously described (Becker et al., 2010).

Phosphorylated and total STAT5 was stained as follows: Stimulated CFU-E cells were fixed in Fixation Buffer (BD Biosciences) or 4% PFA in PBS. Cells were permeabilized in ice-cold Perm Buffer III (BD Biosciences) or 90% methanol. Prior to acquisition, cells were washed with Stain Buffer (BD Biosciences) or 0.3% BSA/PBS. pSTAT5 was detected with rabbit anti-mouse phospho-STAT5 antibodies, total STAT5 was detected with goat anti-mouse Stat5 antibodies and total SHP1 was detected with rabbit anti-mouse SHP1 antibodies. The secondary antibodies were anti-rabbit coupled to APC for pSTAT5 and SHP1, and anti-goat coupled to FITC for total STAT5.

Co-staining of phosphorylated STAT5 and phosphorylated STAT1 or phosphorylated STAT3 was performed as follows: CFU-E cells were fixed in 4% PFA in PBS. Cells were permeabilized in ice-cold 90% methanol. Prior to acquisition, cells were washed with 0.3% BSA/PBS. pSTAT5 was detected with anti-pSTAT5 antibodies coupled to Pacific Blue, pSTAT1 was detected with anti-pSTAT1 antibodies coupled to Alexa Fluor 488 and pSTAT3 was detected with anti-pSTAT3 antibodies coupled to Alexa Fluor 488. Flow cytometry was performed on a BD FACSCanto II flow cytometer (BD Biosciences). Recorded files were exported and subsequently analyzed with FlowJo V.10.0.8.

Cell fractionation

For fractionation of cytoplasmic and nuclear lysates, CFU-E cells were treated with 2 × Homogenization buffer 1 (1 × buffer: 0.1mM EDTA, 0.1mM EGTA, 10mM NaF, 10 mM HEPES pH 7.9, 10 mM KCl, 1 mM DDT, 1 mM NaV_3VO_4) supplemented with 2 μg/ml aprotinin and 200 μg/ml AEBSF. Upon addition of 1 × Homogenization buffer 1 supplemented with 5% NP-40, samples were incubated for 5 min on ice and then centrifuged for 3 min at 14,000 rpm and 4°C. Supernatant was taken as cytoplasmic fraction. Remaining pellets were washed three times with 1 × Homogenization buffer 1 and subsequently re-suspended in 1 × Homogenization buffer 2 (400 mM NaCl, 1 mM EDTA, 1 mM EGTA, 10 mM NaF, 10 mM HEPES pH 7.9, 1 mM DDT, 1 mM NaV_3VO_4) supplemented with 1 μg/ml aprotinin and 100 μg/ml AEBSF. Samples were shaken at 1,400 rpm and 4°C for 1 h, sonicated for 30 s and then centrifuged for 20 min at 14,000 rpm and 4°C. The supernatant was taken as nuclear fraction.

Quantitative immunoblotting, qPCR and mass spectrometry

Quantitative immunoblotting, qPCR and mass spectrometry was performed as described earlier (Bachmann et al., 2011).

METHOD DETAILS

Mathematical modeling of population-average data

While computational frameworks for the quantitative dynamical modeling of population-level data are well established (Balsa-Canto and Banga, 2011; Hoops et al., 2006; Raue et al., 2015), mechanistic modeling of single-cell data remains challenging. Available approaches for the mechanistic description of cell-to-cell variability include stochastic modeling for gene expression (Neuert et al., 2013), mixed-effect modeling for signal transduction (Karlsson et al., 2015) and a variety of hybrid approaches (Fröhlich et al., 2018; Loos et al., 2018; Toni and Tidor, 2013; Zechner et al., 2012). However, these mathematical modeling techniques are computationally very demanding, which renders model establishment and comparison challenging. Therefore, it was of importance to establish a method that enables efficient and yet accurate parameter estimation in single-cell models. For the calibration of such mathematical models, appropriate quantitative experimental data are required. Recently, single-cell RNA sequencing approaches have been utilized (Buettner et al., 2015; Dalerba et al., 2011) to study gene expression in single cells. Clustering algorithms facilitated the identification of distinct cell populations based on these datasets. While these data could also be employed to analyze cell-to-cell variability in a specific cell population, usually only a few hundred unique transcripts are sequenced per cell, limiting the resolution of these methods.

More importantly, since it has been shown that the correlation between mRNA expression levels and protein abundance is low (Schwanhäusser et al., 2011) and intracellular information processing, which links e.g., changes in ligand concentration to cell fate decisions, is executed by complex non-linear reaction networks, it is essential to assess alterations of proteins at the single-cell level. While single-cell time-lapse microscopy allows to follow changes in proteins in individual cells over time, options for monitoring signal transduction components and multiplexing are limited in this technique because only few fluorophores for simultaneous quantification are available and the required tagging with fluorophores might change the properties of proteins (Weill et al., 2019). In contrast, flow cytometry and mass cytometry enable snapshot measurements of dozens of markers in individual cells (Bodenmiller et al., 2012; Perfetto et al., 2004).

Model topology and data integration

The published ordinary differential equations (ODEs) and the corresponding experimental data (Bachmann et al., 2011) were used as a basis for the mathematical modeling. To ensure comparability on absolute scales with the mixed-effect models, parameter transformations implemented in the published model were avoided. To focus the analysis, we neglected the nine data points for the CIS overexpression condition and removed the mechanism of unspecific binding of CIS to EpoR in the absence of Epo. These adaptions reduced the computational effort when simulating the model output without dropping any other key features of the original model. Complementary, the error of relative pSTAT measured by mass spectrometry was kept constant to 5.55% as previously defined (Boehm et al., 2014; Hahn et al., 2013).

The fluorescence intensities recorded in the flow cytometry experiments were transformed to logicle scale (Ellis et al., 2018), which is a biexponential scale and allows to deal with negative values resulting from compensation (Herzenberg et al., 2006; Moore and Parks, 2012; Parks et al., 2006):

$$logicle_{a,b,c,d,f}(x) = a\,exp(bx) - c\,exp(-dx) + f.$$

The coefficients a, b, c, d, and f are determined from the following quantities, which only depend on the dataset:

- T: Top of the data scale. We used $T = 2^{18}$.
- W: Width of the data range in approximately linear scale in decades. We used $W = 0.74$ as suggested in Moore and Parks (2012).
- M: Width of data range in approximately logarithmic scale in decades. We used $M = 4.5$, as suggested in Moore and Parks (2012).

- $\boldsymbol{A}$: Additional width of data range in negative scale. We used $\boldsymbol{A} = \mathbf{0}$, which reproduces the standard logicle scale as introduced in Parks et al. (2006).

We employed a MATLAB implementation which determines the coefficients a, b, c, d, and f directly from T, M, W, and A according to Moore and Parks (2012).

Utilization of this scale is common practice for the visualization and statistical analysis of flow cytometry data and is specifically useful for cases in which negative values appear after background correction of the raw data and when a more accurate representation of the distribution of intensities around zero is favorable. While the traditional logarithmic scaling of the fluorescence intensities yields a clear data distribution for higher values, it cannot cope with negative values and it tends to 'piling up' of intensities on the lower end of the scale. By construction, the logicle scale is able to combine the advantages of the logarithmic scale for higher values with a linear-like scale for the lower end.

For each time point and Epo dose the mean of the logicle scale-transformed fluorescence intensities was used as data point for the fitting of the population-average model. For the quantitative immunoblotting, real-time PCR and mass spectrometry experiments the measured intensities, which should correspond to the mean of the measured cell population, were considered as data points.

Parameter estimation and profile likelihood

All calculations and analyses of the ODE system describing the pathway model were done within the MATLAB-based modeling environment D2D (https://data2dynamics.github.io/d2d/) (Raue et al., 2015). The ODEs were solved by a parallelized implementation of the CVODES initial value problem solver (Hindmarsh et al., 2005). The ODE model was calibrated using maximum likelihood estimation (Raue et al., 2015). We used the local deterministic Gauss-Newton gradient-based trust-region optimizer implemented in the MATLAB function lsqnonlin which is part of the MATLAB optimization toolbox. Multi-start optimization runs with in each case at least 2500 initial guesses were performed using the afore-described model and dataset as well as for each reduced model (see section Model reduction). To assess the uncertainty and identifiability of the estimated parameters the profile likelihood (Raue et al., 2009, 2010) was calculated using D2D. We used profile likelihood analysis rather than Markov-chain Monte Carlo (MCMC)-based uncertainty quantification, as the profile likelihood method tends to be more robust in the case of non-identifiable parameters (Raue et al., 2012a). For models without non-identifiable parameters, it has been shown to provide similar results, while being faster to compute than MCMC methods (Simpson et al., 2020).

Model reduction

Based on the comprehensive experimental dataset and the original population-average model topology, a systematic data-based model reduction was performed by iteratively analyzing the profile likelihood (Hass et al., 2017; Maiwald et al., 2016; Tönsing et al., 2018). By this, non-identifiabilities can be resolved without changing the dynamics of the observed model entities.

First, we observed the inverse coupling of the non-identifiable parameters for the activation rate of SHP1 by the active form of the EpoRJAK2 (EpoRpJAK2 and pEpoRpJAK2) complex and the rate by which the pEpoRpJAK2 state is recycled to its deactivated form by activated SHP1 (SHP1Act). This suggests a weak activation of SHP1. Analogously to scenario 3 in Maiwald et al. (2016), the SHP1 activation is so weak that it merely changes the level of the inactive SHP1 state, although the amount of active SHP1 is not negligible, as it mediates the deactivation of the EpoRJAK2 receptor. As a result, the profile likelihood of the activation rate is open to minus infinity on the $\log_{10}$ scale, i.e., to zero on the linear scale, while the SHP1Act mediated deactivation rate compensates for this and its profile is open to infinity. We resolved this non-identifiability by reparametrizing the SHP1 mediated deactivation rate with the inverse of the SHP1 activation rate, which yields the new, practically identifiable parameter DeaEpoRJAKActSHP1 and structural non-identifiability of the SHP1 activation rate. The latter is resolved by fixing it to an arbitrary value, which in the end is equivalent to a constant SHP1 state with fixed functional relation between SHP1 and its active form.

Second, we observed the non-identifiability of the CISmRNA turnover parameter (CISRNATurn) with a profile likelihood open to infinity. This parameter is related to the modeling of a transcriptional delay in the synthesis of CISmRNA via the linear chain trick (MacDonald, 1976). We resolved this non-identifiability by iteratively reducing the chain length from five to two.

Thirdly, we observed that the SOCS3mRNA transcription process showed a similar behavior in the SOCS3mRNA turnover parameter (SOCS3TurnRNA) and the corresponding delay parameter (SOCS3RNADelay), as well as the SOCS3 translational process in the parameter (SOCS3Turn). All three model parameters showed a practically non-identifiability with profile likelihoods open to infinity. This implies that the measured data of SOCS3 mRNA and SOCS3 protein can be described by the model without delay but a single step. This is consistent with the experimental data for SOCS3 mRNA and SOCS3 protein, which do not indicate a delay. As a consequence, the transcriptional delay, the transcriptional and the translational process of the synthesis of SOCS3 were merged into one single reaction.

The three model reduction steps yielded a model with only two remaining practically non-identifiable parameters: the rate of Epo receptor mediated STAT5 phosphorylation (STAT5ActEpoR) and the parameter capturing the inhibition STAT5 phosphorylation by CIS (CISInh). These parameters cannot be determined from the available experimental data, but related studies showed the relevance of these processes (Gobert et al., 1996; Yoshimura et al., 1995). To ensure biological plausibility of the model and because these non-identifiabilities do not diminish the predictive power of the model's output, we did not perform an additional model reduction step.

The different parameter and state eliminations provide a reduced model (see Model equations below) which captures the core features of the original model and is able to describe all available population-average data. However, the identifiability of the remaining model parameters improved considerably when compared to the model suggested from Bachmann et al. (2011) and provides finite profile likelihood-based confidence intervals at a confidence level of 0.95 for 19 of the 21 dynamic parameters. At a confidence level of 0.68, all dynamic parameters have finite profile likelihood-based confidence intervals. In addition, the described model reduction resulted in a substantial improvement of optimizer performance and convergence. On average 4.1 fits per hour converged to the global optimum for the reduced model and the complete dataset, whereas only 2.6 fits per hour converged to the global optimum for the initial model structure. All fits belonged to a multi-start sequence with 5000 initial guesses on a 16-core @ 2.4 GHz CPU.

Model equations

Set of ordinary differential equations (ODEs) for the reduced model:

$$\frac{d[EpoRJAK2]}{dt} = -\frac{[Epo]\cdot[EpoRJAK2]\cdot JAK2ActEpo}{[SOCS3]\cdot SOCS3Inh+1} + \frac{[EpoRpJAK2]\cdot[SHP1Act]\cdot DeaEpoRJAKActSHP1}{SHP1ActEpoR}$$

$$+\frac{[SHP1Act]\cdot DeaEpoRJAKActSHP1\cdot[p1EpoRpJAK2]}{SHP1ActEpoR}$$

$$+\frac{[SHP1Act]\cdot DeaEpoRJAKActSHP1\cdot[p2EpoRpJAK2]}{SHP1ActEpoR}$$

$$+\frac{[SHP1Act]\cdot DeaEpoRJAKActSHP1\cdot[p12EpoRpJAK2]}{SHP1ActEpoR}$$

$$\frac{d[EpoRpJAK2]}{dt} = \frac{[Epo]\cdot[EpoRJAK2]\cdot JAK2ActEpo}{[SOCS3]\cdot SOCS3Inh+1} - \frac{[EpoRpJAK2]\cdot[SHP1Act]\cdot DeaEpoRJAKActSHP1}{SHP1ActEpoR}$$

$$-\frac{EpoRActJAK2\cdot[EpoRpJAK2]}{[SOCS3]\cdot SOCS3Inh+1} - \frac{3\cdot EpoRActJAK2\cdot[EpoRpJAK2]}{[SOCS3]\cdot SOCS3Inh+1}$$

$$\frac{d[p1EpoRpJAK2]}{dt} = \frac{EpoRActJAK2\cdot[EpoRpJAK2]}{[SOCS3]\cdot SOCS3Inh+1} - \frac{3\cdot EpoRActJAK2\cdot[p1EpoRpJAK2]}{[SOCS3]\cdot SOCS3Inh+1}$$

$$-\frac{[SHP1Act]\cdot DeaEpoRJAKActSHP1\cdot[p1EpoRpJAK2]}{SHP1ActEpoR}$$

$$\frac{d[p2EpoRpJAK2]}{dt} = \frac{EpoRActJAK2\cdot[EpoRpJAK2]}{[SOCS3]\cdot SOCS3Inh+1} - \frac{EpoRActJAK2\cdot[p2EpoRpJAK2]}{[SOCS3]\cdot SOCS3Inh+1}$$

$$-\frac{[SHP1Act]\cdot DeaEpoRJAKActSHP1\cdot[p2EpoRpJAK2]}{SHP1ActEpoR}$$

$$\frac{d[p12EpoRpJAK2]}{dt} = \frac{3\cdot EpoRActJAK2\cdot[p1EpoRpJAK2]}{[SOCS3]\cdot SOCS3Inh+1} + \frac{EpoRActJAK2\cdot[p2EpoRpJAK2]}{[SOCS3]\cdot SOCS3Inh+1}$$

$$-\frac{[SHP1Act]\cdot DeaEpoRJAKActSHP1\cdot[p12EpoRpJAK2]}{SHP1ActEpoR}$$

$$\frac{d[SHP1Act]}{dt} = SHP1^{init} \cdot SHP1ActEpoR \cdot ([EpoRpJAK2] + [p12EpoRpJAK2] + [p1EpoRpJAK2] + [p2EpoRpJAK2]) - [SHP1Act] \cdot SHP1Dea$$

$$\frac{d[STAT5]}{dt} = [STAT5] \cdot STAT5ActJAK2 \cdot \frac{[EpoRpJAK2] + [p12EpoRpJAK2] + [p1EpoRpJAK2] + [p2EpoRpJAK2]}{[SOCS3] \cdot SOCS3Inh + 1} - \frac{[STAT5] \cdot STAT5ActEpoR \cdot ([p12EpoRpJAK2] + [p1EpoRpJAK2])^2}{([CIS] \cdot CISInh + 1) \cdot ([SOCS3] \cdot SOCS3Inh + 1)} + STAT5Exp \cdot [npSTAT5] \cdot \frac{0.275}{0.4}$$

$$\frac{d[pSTAT5]}{dt} = [STAT5] \cdot STAT5ActJAK2 \cdot \frac{[EpoRpJAK2] + [p12EpoRpJAK2] + [p1EpoRpJAK2] + [p2EpoRpJAK2]}{[SOCS3] \cdot SOCS3Inh + 1} + \frac{[STAT5] \cdot STAT5ActEpoR \cdot ([p12EpoRpJAK2] + [p1EpoRpJAK2])^2}{([CIS] \cdot CISInh + 1) \cdot ([SOCS3] \cdot SOCS3Inh + 1)} - STAT5Imp \cdot [pSTAT5]$$

$$\frac{d[npSTAT5]}{dt} = STAT5Imp \cdot [pSTAT5] \cdot \frac{0.4}{0.275} - STAT5Exp \cdot [npSTAT5]$$

$$\frac{d[CISnRNA1]}{dt} = CISRNAEqc \cdot CISRNATurn \cdot [npSTAT5] \cdot (ActD - 1) - CISRNADelay \cdot [CISnRNA1]$$

$$\frac{d[CISnRNA2]}{dt} = CISRNADelay \cdot [CISnRNA1] - CISRNADelay \cdot [CISnRNA2]$$

$$\frac{d[CISRNA]}{dt} = CISRNADelay \cdot [CISnRNA2] \cdot \frac{0.275}{0.4} - [CISRNA] \cdot CISRNATurn$$

$$\frac{d[CIS]}{dt} = CISEqc \cdot [CISRNA] \cdot CISTurn - [CIS] \cdot CISTurn$$

$$\frac{d[SOCS3]}{dt} = SOCS3Eqc \cdot SOCS3Turn \cdot [npSTAT5] - [SOCS3] \cdot SOCS3Turn + SOCS3Turn \cdot SOCS3oe$$

Initial values of ODE system:

$$\begin{gathered}
CIS(t=0) = CIS^{init} = 0 \\
CISRNA(t=0) = CISRNA^{init} = 0 \\
CISnRNA1(t=0) = CISnRNA1^{init} = 0 \\
CISnRNA2(t=0) = CISnRNA2^{init} = 0 \\
EpoRpJAK2(t=0) = EpoRpJAK2^{init} = 0 \\
SHP1Act(t=0) = SHP1Act^{init} = 0 \\
SOCS3(t=0) = SOCS3^{init} = 0 \\
npSTAT5(t=0) = npSTAT5^{init} = 0 \\
p12EpoRpJAK2(t=0) = p12EpoRpJAK2^{init} = 0 \\
p1EpoRpJAK2(t=0) = p1EpoRpJAK2^{init} = 0 \\
p2EpoRpJAK2(t=0) = p2EpoRpJAK2^{init} = 0 \\
pSTAT5(t=0) = pSTAT5^{init} = 0
\end{gathered}$$

Applied parameter transformations:

$$CISInh \rightarrow \frac{CISInh}{CISEqc}$$

$$SOCS3Inh \rightarrow \frac{SOCS3Inh}{SOCS3Eqc}$$

An implementation of these equations is available in SBML format within the Biomodels repository:MODEL2103080001.

Mixed-effect modeling for cell population

In this study we account for cell-to-cell variability be allowing the protein abundances and parameters of individual cells to differ. This is a common approach to capture (slow) extrinsic noise. As shown in Bachmann et al. (2011), the abundance of most biochemical species involved in the process is rather high. In particular, validation using the stochastic simulation algorithm (Gillespie, 1977) showed a negligible effect of stochastic dynamics (or intrinsic noise) for phosphorylated cytoplasmic and nuclear STAT5. Hence, we assumed that the overall influence of intrinsic noise (stochasticity of cellular processes causing differences) is minimal. Mathematically, considering differences between the parameters of individual cells yield a mixed-effect model of the process. As we propagate this model through an ODE – providing a non-linear map from parameters to outputs –, we obtain a nonlinear mixed-effect model (NLMEM).

To simulate the NLMEM, we create an *in-silico* population of cells, in which each single-cell has its own parameter vector. The parameter vector ϕ^i for the i-th cell is given as

$$\phi^i = F\beta + Rb^i,$$

in which F and R are called design matrices for fixed and random effects, $\beta \in R^{n_\beta}$ is the vector of fixed effects (i.e., the parameter set describing the population mean), $b^i \in R^{n_b}$ is the vector of random effects for the i-th cell. The fixed effects β influence the parameters of all cells, while the random effects b^i are specific to one single-cell. We assume the random effects to follow a multivariate normal distribution with mean 0 and covariance matrix Σ, $b^i \sim N(0, \Sigma)$. The covariance matrix Σ is parameterized by a vector δ, yielding the parameter vector $\theta = (\beta, \delta)$, which describes the population dynamics. Hence, the parameter estimation problem of the population-average model (where only β has to be inferred) is extended for the mixed effect model by the parameters of the population distribution which are grouped in δ.

The term "NLMEM" is typically used when analyzing single-cell time-lapse data (Karlsson et al., 2015), however, many of the models used for single-cell snapshot data are also NLMEM (Loos et al., 2018). As the cells from different time points in a time series of flow cytometry data are not the same and are hence not directly comparable, we did not fit single-cell trajectories to the whole dataset. Instead, we simulated a heterogeneous population, propagated it through the ODE and fitted the shapes of the simulated distributions of certain protein abundances to the snapshots. As a measure of the shape of these distributions, we used means, variances, and covariances.

In more detail, this means that for a population with M individuals, we simulated M trajectories of state variables

$$x^i(t) = \int_{t_0}^{t} f\left(s, x\left(s, \phi^i\right), \phi^i\right) ds$$

for each random effect vector b^i, where f is the vector field of the considered ODE model: $\dot{x}^i(t) = f\left(t, x^i(t), \phi^i\right)$ with $x^i(t_0) = x_0(\phi^i)$. This yielded M trajectories of observables

$$y^i(t) = h\left(x^i(t), \phi^i\right)$$

from which the means, variances, and the covariances (and possibly higher moments) can be computed and fitted to measurement data.

Approximations to simulate cell populations

A faithful representation of the cell-to-cell variability at a given time point in a cell population had to be balanced with computational costs of the utilized multi-start parameter estimation. Because the number of molecules ranged from around 1,000 molecules for the EpoR to around 20,000 molecules per cell for STAT5 (Bachmann et al., 2011) and was therefore sufficiently large, we employed a deterministic mixed-effect modeling approach (Fröhlich et al., 2017). Mixed-effect modeling allowed each parameter to be either fixed or variable across cells. Parameters, which are assumed to be variable across cells, were referred to as "random effects," otherwise they were called "fixed effects." Random effects should follow a multivariate normal distribution, which was parametrized by the population mean and a covariance matrix. Hence, compared to the population-average JAK2/STAT5 model, the single-cell JAK2/SAT5 model was extended by additional degrees of freedom, which parametrize the covariance matrix of the random effects.

The calibration of the single-cell model was computationally much more demanding, because (i) the additional degrees of freedom increased the dimensionality of the estimation problem, and (ii) the evaluation of the cell-population dynamics required a large number of single-cell simulations, with parameters sampled from the multivariate normal distribution. Hence, we had to improve the feasibility of previously proposed approximation methods. The key challenge was the computational complexity of simulating the population dynamics, a step which needs to be repeated during every step of the model calibration. To reduce the computational costs, the mean and the covariance can be approximated using sigma points (Loos et al., 2018; Toni and Tidor, 2013). However, as shown in Figure 3A, this method possesses a low accuracy for the considered problem.

Thus, we introduced a Dirac-mixture distribution (Gilitschenski and Hanebeck, 2013), which allows for a high approximation accuracy via the specification of an appropriate number of samples. The sample points were chosen such that the corresponding Dirac-mixture distribution provided an accurate approximation of the multivariate normal distribution (Hanebeck and Klumpp, 2008) describing cell-to-cell variability (Figure 3B). We used 42 sample points for this approximation, thus we required about 250 times fewer simulations than for a corresponding Monte-Carlo-based trajectory (Figure 3C). Our approach allowed to flexibly balancing the computational complexity, as determined by the number of points, and approximation accuracy. The validity of this approximation, on which all results of the parameter estimation and the model selection relied, was ensured by comparing the final approximate simulations after the model calibration (Figure 3B) to an accurate Monte Carlo simulation with 10,000 samples, which is considered to be as close as possible to the truth (Figure 3C). To further enhance computational efficiency and optimizer convergence, we derived the respective forward sensitivity equations for the gradient calculations, optimized logicle- and log-transformed parameters and developed a parametrization approach for the covariance matrix (for details, see below).

Monte Carlo sampling

The simplest way to approximate the means, variances, and the covariances is to directly simulate a cell population using parameters obtained from Monte Carlo sampling. For each individual cell $i \in 1,\ldots,M$, the random effect vector b^i is given by

$$b^{i,Samp} = \psi_b^{Samp}(i, M, \Sigma) := L\varepsilon^i,$$

in which L is the lower factor of the Cholesky decomposition of covariance matrix Σ and ε^i is th i-th sample from a set of M standard normally distributed points in R^{n_b}. Outputs like mean and covariance of observables are obtained from the outputs of each sample.

The size M of the sampled population must be large enough to reflect the behavior of the distribution function. For this purpose, sample sizes of e.g., 10,000 simulated cells are common, which means that the computation time necessary for model parametrization must be multiplied with the size of the cell population. While this may be feasible for analytic or very simple ODE models, it is computationally intractable for the model considered in this work, since this would result in millions of hours of computation time. However, simulating a full population of cells represents the most faithful method for describing the actual biological system. Hence, we compared the final simulation results obtained from other approximation methods regularly to simulation results obtained using Monte Carlo sampling.

Sigma point methods

The sigma point approach (van der Merwe, 2004) is one of the computationally most efficient methods to approximate a population of cells. Given n_b random effects, we need to compute $2n_b + 1$ (sigma) points and propagate them through the ODE. These points are usually located at 0 and $\pm h$ along the parameter axes in each random effect direction, where h is a chosen step size, which is set to $\sqrt{0.5 \cdot n_b}$. If Σ is the unit matrix, this will yield $b^{i,SP} = he_i$ with e_i being the i-th unit vector. In the general case, the sigma points get transformed with the lower Cholesky decomposition of the covariance matrix:

$$\boldsymbol{b}^{i,SP} = \boldsymbol{\psi}^{SP}(\boldsymbol{i}, \boldsymbol{M}, \boldsymbol{\Sigma}) := \boldsymbol{Lhe}_i, \text{ for } \boldsymbol{i} \in \{1, \ldots, \boldsymbol{n_b}\},$$

$$\boldsymbol{b}^{i,SP} = \boldsymbol{\psi}^{SP}(\boldsymbol{i}, \boldsymbol{M}, \boldsymbol{\Sigma}) := -\boldsymbol{Lhe}_i, \text{ for } \boldsymbol{i} \in \{\boldsymbol{n_b} + 1, \ldots, 2\boldsymbol{n_b}\},$$

and

$$\boldsymbol{b}^{0,SP} = 0.$$

Additionally, the sigma points carry weights $\boldsymbol{w}_m^i, \boldsymbol{i} \in \{0, \ldots, 2\boldsymbol{n_b}\}$ for the means and weights $\boldsymbol{w}_C^i, \boldsymbol{i} \in \{0, \ldots, 2\boldsymbol{n_b}\}$ for the covariances. They are computed as:

$$\boldsymbol{w}_m^0 = \frac{\lambda}{\lambda + \boldsymbol{n_b}}$$

$$\boldsymbol{w}_m^i = \frac{1}{2(\lambda + \boldsymbol{n_b})}, \text{ for } \boldsymbol{i} > 0$$

$$\boldsymbol{w}_C^0 = \frac{2\lambda + \boldsymbol{n_b}}{\lambda + \boldsymbol{n_b}} + \boldsymbol{q} - \boldsymbol{a}^2$$

$$\boldsymbol{w}_m^i = \frac{1}{2(\lambda + \boldsymbol{n_b})}, \text{ for } \boldsymbol{i} > 0$$

where we fixed $\boldsymbol{a} = 0.7$ (it should hold: $0 < \boldsymbol{a} \leq 1$), $\boldsymbol{q} = 2$ (it should hold $\boldsymbol{q} \geq 1$) and $\lambda = \boldsymbol{n_b}(\boldsymbol{a}^2 - 1)$. These weights are then used to compute means, variances, and covariances of observables.

Dirac mixture models

The sigma point approximation may be computationally efficient, but it reflects the mean and variance only for linear systems exactly. Therefore, it can be inaccurate for highly nonlinear applications such as nonlinear ODE systems. Since in our case, massive Monte Carlo sampling was computationally infeasible and sigma points approximations provided poor results, we decided to use Dirac mixture distribution (DMD) approximations (Gilitschenski and Hanebeck, 2013). A DMD is a small set of points, which attempts to accurately reflect a multivariate normal distribution by fulfilling an optimality condition on the approximation quality. The number of these Dirac points can be freely chosen, in order to adapt the approximation quality. Thus, a DMD can either be interpreted as a small, but optimal sample, or as a sigma point method with adjustable accuracy. This allowed us to balance computational effort and numerical accuracy with high flexibility. However, this has the disadvantage that the DMD with the desired properties must be computed before it can be used for parameter estimation. To do so, a multivariate standard normal distribution with the desired dimension $\boldsymbol{n_b}$ is approximated by a mixture of $\boldsymbol{n_D}$ Dirac-delta distributions. We decided to use $\boldsymbol{n_D} = 42$, since this yields $\boldsymbol{n_D}/\boldsymbol{n_b} = 6$, which are three times as many points as in the case of the sigma point approximation, which has $\boldsymbol{n_D} = 2\boldsymbol{n_b} + 1$. This guarantees a substantially higher approximation accuracy than the sigma point approximation.

The DMD for the smaller models ($\boldsymbol{n_b} = 6$ and $\boldsymbol{n_b} = 4$) were computed from the largest one by integrating out the corresponding columns. In this way, we could make sure that the calibrated models are really nested and can be analyzed with means such as the BIC. Otherwise, slightly different approximation accuracies due to different numbers of mixture points can dominate the parameter estimation results and may lead to incorrect conclusions when applying model criteria such as the BIC.

In order to compute the locations of the $\boldsymbol{n_D}$ Dirac-points $\boldsymbol{z} = (\boldsymbol{z}_1, \ldots, \boldsymbol{z}_{\boldsymbol{n_D}}) \in \boldsymbol{R}^{\boldsymbol{n_b} \times \boldsymbol{n_D}}$, a modified Cramér-von Mises-distance between distributions is defined based on a measure called localized cumulative distribution (LCD) (Hanebeck and Klumpp, 2008). The LCD is a substitute for the cumulative distribution for multivariate probability density functions. For an $\boldsymbol{n_b}$-dimensional probability density function $\boldsymbol{f} : \boldsymbol{R}^{\boldsymbol{n_b}} \to \boldsymbol{R}^+$, the corresponding LCD is defined as

$$\boldsymbol{F_f}(\boldsymbol{m}, \boldsymbol{B}) = \boldsymbol{p_f}\left(\boldsymbol{x_i} - \boldsymbol{m} \vee \leq \frac{1}{2}\boldsymbol{B_i}\right)$$

with $\boldsymbol{B} \in \boldsymbol{R}^{\boldsymbol{n_b},+}$, $\boldsymbol{m} \in \boldsymbol{R}^{\boldsymbol{n_b},+}$ and $\boldsymbol{p_f}$ being the probability given the density function $\boldsymbol{f}$. This is used to define a (so-called modified Cramér-von Mises) distance between two densities $\boldsymbol{f}$ and $\boldsymbol{g}$ in the following way:

$$\boldsymbol{D}_\omega(\boldsymbol{f}, \boldsymbol{g}) = \int_{\boldsymbol{R}^{\boldsymbol{n_b}}} \int_{\boldsymbol{R}^{\boldsymbol{n_b},+}} \omega(\boldsymbol{m}, \boldsymbol{B}),$$

where an additional weighting function ω can be used.

We chose $\boldsymbol{f}$ to be a multivariate standard normal distribution $\boldsymbol{N}(0,1)$ with dimension $\boldsymbol{n_b} = 7$, and $\boldsymbol{g}$ to be a $\boldsymbol{DMD}(\boldsymbol{z})$ with $\boldsymbol{n_D} = 42$ points at the locations $\boldsymbol{z^i}, \boldsymbol{i} = 1, \ldots, \boldsymbol{n_D}$ and the weighting to

$$\omega(\boldsymbol{m}, \boldsymbol{B}) = \begin{cases} (\boldsymbol{B^i})^{1-\boldsymbol{n_b}}, & \boldsymbol{B^i} \in [0,3] \\ 0, & \boldsymbol{otherwise} \end{cases}$$

Then we optimized these locations in order to minimize the distance $\boldsymbol{D}$ and obtained the Dirac points for a standard normal distribution:

$$\boldsymbol{b^{i,DMD,SN}} = \boldsymbol{argmin_z}(\boldsymbol{D}_\omega(\boldsymbol{N}(0,1), \boldsymbol{DMD}(\boldsymbol{z}))).$$

Once the DMD points $\boldsymbol{b^{i,DMD,SN}}$ were computed, they can be transformed with the lower Cholesky decomposition $\boldsymbol{L}$ of the covariance matrix Σ

$$\boldsymbol{b^{i,DMD}} = \boldsymbol{L}\boldsymbol{b^{i,DMD,SN}},$$

and all computations are carried out in the same way as for Monte Carlo sampling.

Parametrizations of covariance matrices

To parametrize the covariance matrices Σ of the random effects, we tested different approaches, as described in Pinheiro and Bates (1996):

- A log-matrix parametrization, in which a symmetric matrix $\boldsymbol{R}$ is parametrized, which fulfils $\Sigma = \boldsymbol{exp}(\boldsymbol{R})$.
- The Givens parametrization, in which the eigenvalues are parametrized logarithmically as a diagonal matrix $\Lambda = \boldsymbol{diag}(\boldsymbol{exp}(\lambda_1, \ldots, \lambda_{n_b}))$ and the system of eigenvectors is parametrized as a product of $\boldsymbol{n_u} = \boldsymbol{n_b}(\boldsymbol{n_b} - \boldsymbol{1})/\boldsymbol{2}$ rotations $\boldsymbol{U}(\varphi_1, \ldots, \varphi_{n_u}) = \prod_{i=1}^{n_u} \boldsymbol{u}_i(\varphi_i)$, where the $\varphi_i \in [\boldsymbol{0}, \pi]$ are rotation angles. This yields $\Sigma = \boldsymbol{U}^T \Lambda \boldsymbol{U}$.

Since none of these methods led to satisfactory results, we designed an approach based on Lie-theoretic considerations: We parametrized the eigenvalues logarithmically as diagonal matrix

$$\Lambda = diag\left(exp\left(\lambda_1, \ldots, \lambda_{n_b}\right)\right)$$

and defined

$$\Sigma = U^T \Lambda U$$

with U being a rotational matrix. However, we parametrized U not directly, as done in the Givens-formula, but indirectly, via the Lie algebra of the rotation group $SO(n)$, i.e., we set

$$U = exp(A), \text{ with } = -A^T,$$

which we assume to have entries $A_{ij} \in [-b, b]$, $with\, b \gg 1$, where b is an arbitrarily chosen bound, for which we used $b = 20$. Thus, we only need to parametrize the antisymmetric matrix A, which is a much simpler task than parametrizing the rotations.

This approach takes advantage of the fact that the exponential map is a local diffeomorphism around the unit elements of the Lie group and the Lie algebra. Furthermore, $A = 0$ being a natural initial guess for the optimization problem, lies at the center of the parameter interval. Compared to the Givens parametrization, this has the advantage of reducing the dependence of the φ_i on each other and hence improving the optimizer convergence.

Parameter estimation for the single-cell models

The parameter estimation for the single-cell models was carried out using the MATLAB-based toolbox PESTO (Stapor et al., 2018). Model calibration was performed using the trust-region-reflective algorithm of the function fmincon (MATLAB Release 2017a), which is part of the MATLAB optimization toolbox. The optimization algorithm was provided with gradients and the Fisher information matrix from forward sensitivity analysis. The mixed-effect model, the different methods for parametrizing the covariance matrix of random effects, and the corresponding sensitivities were constructed using the MATLAB-based toolbox MEMOIR (Fröhlich et al., 2018). MEMOIR also assembled the objective function, which was passed to PESTO, as the log-posterior function of observing a parameter vector given the experimental data, assuming a Gaussian noise model for the population-average data, and the mean values, variances, and covariances of the single-cell snapshot data. The numerical integration of the ODE systems and their forward sensitivities was carried out using the C++ and MATLAB-based toolbox AMICI (Fröhlich et al., 2017), which interfaces the CVODES solver from the SUNDIALS suite (Hindmarsh et al., 2005).

For Single-Cell Model 1 we considered our previously established concept that intracellular information processing is largely determined by the abundance of signaling components (Adlung et al., 2017) and allowed the initial amount of EpoR, SHP1 and total STAT5 to vary between cells. Additionally, the measured basal phosphorylation of STAT5 was represented by a cell-specific offset param-

eter, which comprised ligand-independent phosphorylation and the background-signal of the secondary antibodies (see Figure 1A). Accordingly, these parameters of an individual cell were a combination of fixed and random effects, while all other parameters were only defined by fixed effects. To account for interdependencies between the initial amount of EpoR, SHP1 and total STAT5 as well as the pSTAT5 offset (i.e., basal activation plus measurement background), we estimated variances as well as the full covariance structure of the random effects (Figure 4B, blue).

In Single-Cell Model 2 we additionally assumed that the nucleocytoplasmic import and export rate constants are variable between cells, since we showed previously that due to the rapid nucleocytoplasmic cycling behavior of STAT5, both the nucleocytoplasmic import and export rates strongly influence the transcriptional yield of nuclear pSTAT5 (Swameye et al., 2003). This could be due to cell-to-cell variability in the cytoplasmic and nuclear volumes of CFU E cells, which influences the effective import and export rates of individual CFU-E cells. We estimated covariances between these two parameters to account for their correlation, but we disregarded possible interdependencies between the translocation rate constants and other entries of the covariance matrix to limit the overall complexity (Figure 4B, green).

In Single-Cell Model 3, we further allowed the input Epo to vary between cells, since we previously observed rapid receptor-mediated ligand internalization (Becker et al., 2010) and therefore considered the possibility of an uneven distribution of the ligand in the medium or differential ligand accessibility of individual CFU-E cells. We considered the random effect of Epo to be independent from the other cell-to-cell variabilities (Figure 4B, orange).

Each of the three single-cell models was calibrated by multi-start local optimization with analytical gradient information of the aforementioned approximation using Dirac-mixture distributions. In addition to the population-average data used for the population-average model (Figures 4C–4E, upper panels), the three single-cell models were also parameterized using variances of total STAT5 and pSTAT5 (Figures 4C–4E, bottom panels), and their covariances, and the means of total STAT5 as measured by flow cytometry, which comprised a total of 960 additional data points. As demonstrated in Figure 4F, the optimizations for all three single-cell models converged well. We performed model selection using the Bayesian information criterion (BIC) (Schwarz, 1978) and found that Single-Cell Model 2 provides an appropriate balance between goodness-of-fit and model complexity (Figure 4G). The optimal values of the log-likelihood functions for Single-Cell Model 2 and 3 were identical, and the difference of 7.5 in the BIC values was due to the penalization of the additional parameters of Single-Cell Model 3. The additional random effect of Epo implemented in Single-Cell Model 3 did not improve the model's performance. Overall, there was a good agreement and high correlation ($\rho = 0.974$; see Figures S4C and S4D) between model simulations and experimental data (Figures 4C–4E), but the single-cell model output was markedly improved by assuming cell-to-cell variability in the import rate of pSTAT5 and the export rate of STAT5 in Model 2 (Figure 4D).

QUANTIFICATION AND STATISTICAL ANALYSIS

Model selection criteria

Model selection for the single-cell models was based on the Bayesian information criterion (BIC) to have a asymptotically consistent model selection criterion. The BIC accounts for the maximum log-likelihood of each model (as a measure for fit quality) and model complexity. The BIC is computed as follows:

$$BIC(M) = -2l\left(\theta_M^{MAP}\right) + n_{\theta_M} log(n_d),$$

where M is the model, l log-posterior (or the log-likelihood) with the maximum *a posteriori* (or maximum likelihood) estimate θ^{MAP}, n_{θ_M} is the number of parameters of M and n_d is the number of data points. Especially for models with many data points (like in our case), the BIC penalizes model complexity stronger than the Akaike information criterion (AIC) and may hence give stronger indications for model selection.

Translocation rates and compartmental volumes

Our single-cell model selection reveals the import and export rates to be variable, and it predicts the heterogeneity of the import rates to be higher than the heterogeneity of the export rates (Figure 6A): In order to quantify this difference more precisely, we used the estimated decadic translocation rate constants $Import_{STAT5}$ and $Export_{STAT5}$ and the estimated covariance matrix of random effects Σ for the simulation of 1,000 cell populations with 100,000 cells each. In this way, we can compute the ratios of the coefficients of variation CV of the rate constants in linear scale for each cell population. This yields for the respective mean values

$$\frac{CV\left(10^{Import_{STAT5}}\right)}{CV\left(10^{Export_{STAT5}}\right)} = \frac{CV(Import\ rate\ constant)}{CV(Export\ rate\ constant)} = 3.9,$$

and a value of 1.6 for the standard deviation of this ratio.

The inverses of the import and export rates on the other hand are proportional to the expected time for a molecule of STAT5 to be imported or exported, respectively (having the unit s/mol or only s, if we consider molecules instead of abundances):

$$10^{-Export_{STAT5}} \propto E(t_{Export}) \text{ and } 10^{-Import_{STAT5}} \propto E(t_{Import})$$

If we assume that molecular transport is driven by diffusion, this expected time for a molecule to be exported should depend on the radius of the cell's nucleus r_{nuc}, which is related to the nucleic volume by $r_{nuc} = \sqrt[3]{\frac{3}{4\pi}V_{cell}}$. On the other hand, we assume the expected

time for a molecule to be imported to depend on the thickness of the cytoplasmic shell t_{cyt} around the nucleus, which is related to the compartmental volume via $t_{cyt} = \sqrt[3]{\frac{3}{4\pi}V_{cell}} - \sqrt[3]{\frac{3}{4\pi}V_{nuc}}$ (see Figure 6B).

Results from the theory of cellular diffusion processes (Bressloff, 2014) state that relations

$$E(t_{Export}) \propto r_{nuc}^2 \text{ and } E(t_{Import}) \propto t_{cyt}^2$$

should hold. We confirmed the first relation by simulating 10,000 random walks in three dimensions with for different nucleic radii (Figure 6C). In such a random walk, which we always started in the center of the nucleus, a molecule could move along each coordinate axis either forward or backward with a fixed step size until it reached the boundary of the nucleic sphere. The mean of the computation times of these random walks was computed and used as a proxy for the expected export time of a STAT5 molecule. For the nuclear import process, we assumed that that $r_{cyt} \ll r_{nuc}$, which allowed us to approximate the import process by a random walk between two planes with distance t_{cyt} in three dimensions. We simulated again 10,000 random walks, which were constraint to stay between the planes, starting at the first one (the cell membrane) and stopped them when the second one (the nucleic membrane) was reached. By carrying out the corresponding computations for different distances between the planes, we also confirmed the second relation (Figure 6C).

Based on these considerations, we conclude that the relation

$$\frac{CV\left(t_{cyt}^2\right)}{CV\left(r_{nuc}^2\right)} \in [2.3, 5.5]$$

should hold. Evaluating the results from confocal fluorescence microscopy z stack images, the corresponding coefficients of variation indeed yielded the ratio

$$\frac{CV\left(t_{cyt}^2\right)}{CV\left(r_{nuc}^2\right)} = 3.1.$$

Inference of the survival criterion

Similar to the work by Bachmann et al. (2011), we compared different criteria for survival against each other. Considered criteria, whether a single-cell would survive, were the total amount of pSTAT5 in the nucleus, which the respective cell is exposed to averaged over the time interval $[0, \boldsymbol{t_{end}}]$. the maximal ratio of pSTAT5 in the nucleus over the total amount of STAT5, which the respective cell is exposed to averaged over the time interval $[0, \boldsymbol{t_{end}}]$.

We checked these two proposed criteria for $\boldsymbol{t_{end}}$ from 5 to 180 min, in steps of 5 min. The necessary thresholds for the respective survival signals were fitted to the survival data based on the selected single-cell model at the optimal parameter value. Since we observe survival also in the absence of Epo, we additionally fitted an offset for this basal survival rate.

The BIC values for these criteria and thresholds yielded that the criteria based on the ratio of pSTAT5 with a threshold $\boldsymbol{t_{end}} = 180$ min was the preferred model for cell survival. The BIC values for the two criteria are shown in Figure S7A.

Cell Reports, Volume *36*

Supplemental information

Cell-to-cell variability in JAK2/STAT5 pathway components and cytoplasmic volumes defines survival threshold in erythroid progenitor cells

Lorenz Adlung, Paul Stapor, Christian Tönsing, Leonard Schmiester, Luisa E. Schwarzmüller, Lena Postawa, Dantong Wang, Jens Timmer, Ursula Klingmüller, Jan Hasenauer, and Marcel Schilling

1 Supplemental Figures

1.1 Figure S1

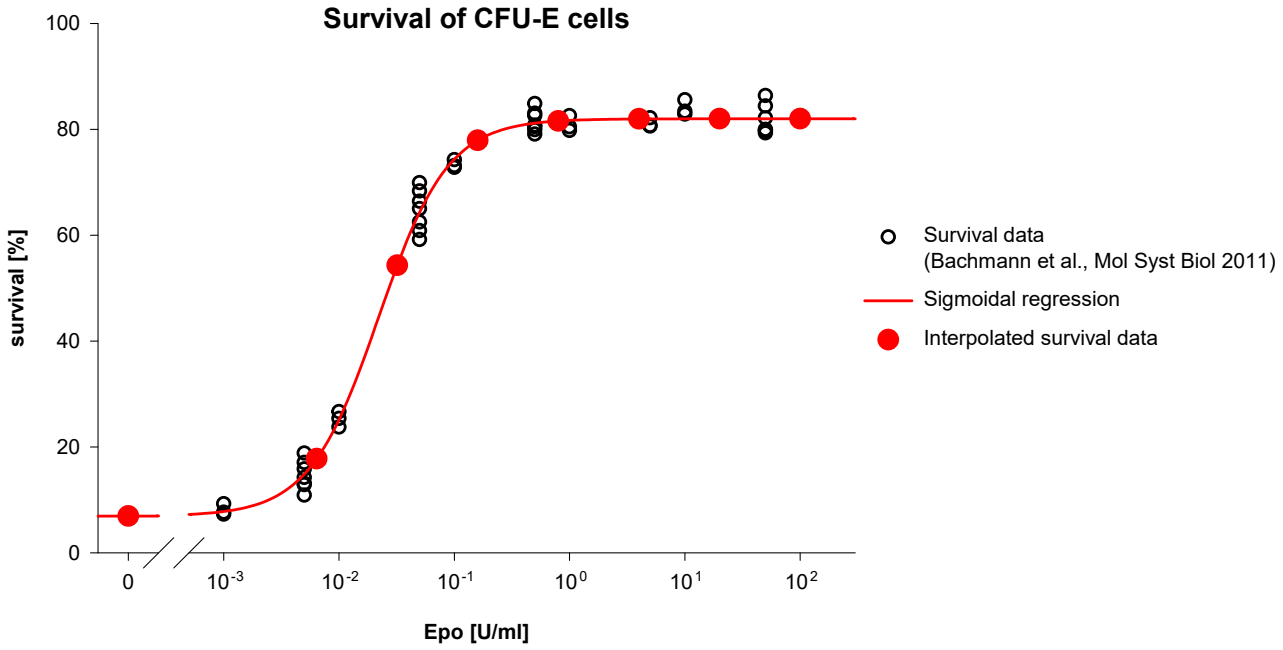

Figure S1 (related to Figure 1): Survival data for CFU-E cells. The percentage of surviving CFU-E cells cultured 24 h in various Epo concentration measured by TUNEL assay as reported in Bachmann et al., Mol Syst Biol 2011 are shown as open black circles. A sigmoidal regression based on a four parameter Hill function was used (solid red line) to interpolate survival data for the Epo concentrations used in Figure 1 (solid red circles).

1.2 Figure S2

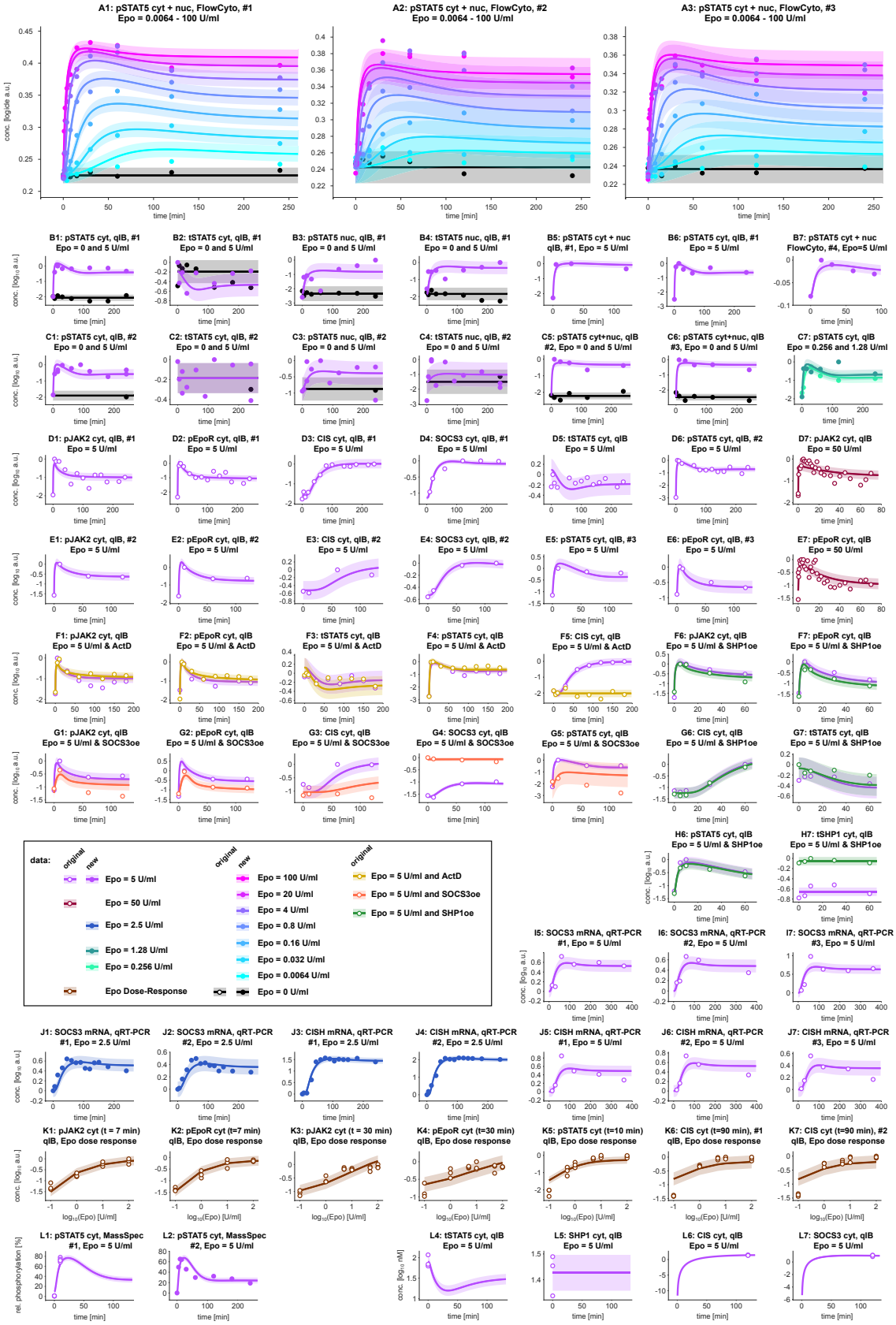
A1: pSTAT5 cyt + nuc, FlowCyto, #1
Epo = 0.0064 - 100 U/ml
A2: pSTAT5 cyt + nuc, FlowCyto, #2
Epo = 0.0064 - 100 U/ml
A3: pSTAT5 cyt + nuc, FlowCyto, #3
Epo = 0.0064 - 100 U/ml
conc. [log\u2081\u2080 a.u.]
time [min]
B1: pSTAT5 cyt, qIB, #1
Epo = 0 and 5 U/ml
B2: tSTAT5 cyt, qIB, #1
Epo = 0 and 5 U/ml
B3: pSTAT5 nuc, qIB, #1
Epo = 0 and 5 U/ml
B4: tSTAT5 nuc, qIB, #1
Epo = 0 and 5 U/ml
B5: pSTAT5 cyt + nuc
qIB, #1, Epo = 5 U/ml
B6: pSTAT5 cyt, qIB, #1
Epo = 5 U/ml
B7: pSTAT5 cyt + nuc
FlowCyto, #4, Epo=5 U/ml
C1: pSTAT5 cyt, qIB, #2
Epo = 0 and 5 U/ml
C2: tSTAT5 cyt, qIB, #2
Epo = 0 and 5 U/ml
C3: pSTAT5 nuc, qIB, #2
Epo = 0 and 5 U/ml
C4: tSTAT5 nuc, qIB, #2
Epo = 0 and 5 U/ml
C5: pSTAT5 cyt+nuc, qIB
#2, Epo = 0 and 5 U/ml
C6: pSTAT5 cyt+nuc, qIB
#3, Epo = 0 and 5 U/ml
C7: pSTAT5 cyt, qIB
Epo = 0.256 and 1.28 U/ml
D1: pJAK2 cyt, qIB, #1
Epo = 5 U/ml
D2: pEpoR cyt, qIB, #1
Epo = 5 U/ml
D3: CIS cyt, qIB, #1
Epo = 5 U/ml
D4: SOCS3 cyt, qIB, #1
Epo = 5 U/ml
D5: tSTAT5 cyt, qIB
Epo = 5 U/ml
D6: pSTAT5 cyt, qIB, #2
Epo = 5 U/ml
D7: pJAK2 cyt, qIB
Epo = 50 U/ml
E1: pJAK2 cyt, qIB, #2
Epo = 5 U/ml
E2: pEpoR cyt, qIB, #2
Epo = 5 U/ml
E3: CIS cyt, qIB, #2
Epo = 5 U/ml
E4: SOCS3 cyt, qIB, #2
Epo = 5 U/ml
E5: pSTAT5 cyt, qIB, #3
Epo = 5 U/ml
E6: pEpoR cyt, qIB, #3
Epo = 5 U/ml
E7: pEpoR cyt, qIB
Epo = 50 U/ml
F1: pJAK2 cyt, qIB
Epo = 5 U/ml & ActD
F2: pEpoR cyt, qIB
Epo = 5 U/ml & ActD
F3: tSTAT5 cyt, qIB
Epo = 5 U/ml & ActD
F4: pSTAT5 cyt, qIB
Epo = 5 U/ml & ActD
F5: CIS cyt, qIB
Epo = 5 U/ml & ActD
F6: pJAK2 cyt, qIB
Epo = 5 U/ml & SHP1oe
F7: pEpoR cyt, qIB
Epo = 5 U/ml & SHP1oe
G1: pJAK2 cyt, qIB
Epo = 5 U/ml & SOCS3oe
G2: pEpoR cyt, qIB
Epo = 5 U/ml & SOCS3oe
G3: CIS cyt, qIB
Epo = 5 U/ml & SOCS3oe
G4: SOCS3 cyt, qIB
Epo = 5 U/ml & SOCS3oe
G5: pSTAT5 cyt, qIB
Epo = 5 U/ml & SOCS3oe
G6: CIS cyt, qIB
Epo = 5 U/ml & SHP1oe
G7: tSTAT5 cyt, qIB
Epo = 5 U/ml & SHP1oe
H6: pSTAT5 cyt, qIB
Epo = 5 U/ml & SHP1oe
H7: tSHP1 cyt, qIB
Epo = 5 U/ml & SHP1oe
data:
original
new
Epo = 5 U/ml
Epo = 50 U/ml
Epo = 2.5 U/ml
Epo = 1.28 U/ml
Epo = 0.256 U/ml
Epo Dose-Response
Epo = 100 U/ml
Epo = 20 U/ml
Epo = 4 U/ml
Epo = 0.8 U/ml
Epo = 0.16 U/ml
Epo = 0.032 U/ml
Epo = 0.0064 U/ml
Epo = 0 U/ml
Epo = 5 U/ml and ActD
Epo = 5 U/ml and SOCS3oe
Epo = 5 U/ml and SHP1oe
I5: SOCS3 mRNA, qRT-PCR
#1, Epo = 5 U/ml
I6: SOCS3 mRNA, qRT-PCR
#2, Epo = 5 U/ml
I7: SOCS3 mRNA, qRT-PCR
#3, Epo = 5 U/ml
J1: SOCS3 mRNA, qRT-PCR
#1, Epo = 2.5 U/ml
J2: SOCS3 mRNA, qRT-PCR
#2, Epo = 2.5 U/ml
J3: CISH mRNA, qRT-PCR
#1, Epo = 2.5 U/ml
J4: CISH mRNA, qRT-PCR
#2, Epo = 2.5 U/ml
J5: CISH mRNA, qRT-PCR
#1, Epo = 5 U/ml
J6: CISH mRNA, qRT-PCR
#2, Epo = 5 U/ml
J7: CISH mRNA, qRT-PCR
#3, Epo = 5 U/ml
K1: pJAK2 cyt (t = 7 min)
qIB, Epo dose response
K2: pEpoR cyt (t=7 min)
qIB, Epo dose response
K3: pJAK2 cyt (t = 30 min)
qIB, Epo dose response
K4: pEpoR cyt (t=30 min)
qIB, Epo dose response
K5: pSTAT5 cyt (t=10 min)
qIB, Epo dose response
K6: CIS cyt (t=90 min), #1
qIB, Epo dose response
K7: CIS cyt (t=90 min), #2
qIB, Epo dose response
conc. [log\u2081\u2080 a.u.]
log\u2081\u2080(Epo) [U/ml]
L1: pSTAT5 cyt, MassSpec
#1, Epo = 5 U/ml
L2: pSTAT5 cyt, MassSpec
#2, Epo = 5 U/ml
L4: tSTAT5 cyt, qIB
Epo = 5 U/ml
L5: SHP1 cyt, qIB
Epo = 5 U/ml
L6: CIS cyt, qIB
Epo = 5 U/ml
L7: SOCS3 cyt, qIB
Epo = 5 U/ml
rel. phosphorylation [%]
conc. [log\u2081\u2080 nM]

Figure S2 (related to Figure 2): Complete data set and model output of population-average model dynamics. Empty circles indicate original data sets from Bachmann et al., Mol Syst Biol 2011, filled circles is new experimental data. All data shown enter the analyses. Model simulations are shown as solid lines in the color of the corresponding experimental conditions. Shading depicts the error model. Measured entities, experimentation techniques, replicate number (rep #) and experimental conditions as indicated in the subplot titles. cyt: only cytopasmatic fraction, nuc: only nuclear fraction, cyt + nuc: whole cell lysates. FlowCyto: Flow cytometry (A1-3, B7), qIB: quantitative immunoblotting (B1-H7, L4-L7), qRT-PCR: quantitative Real-Time Transcription PCR (I5-7, J1-7), MassSpec: Mass spectrometry (L1-L2).

1.3 Figure S3

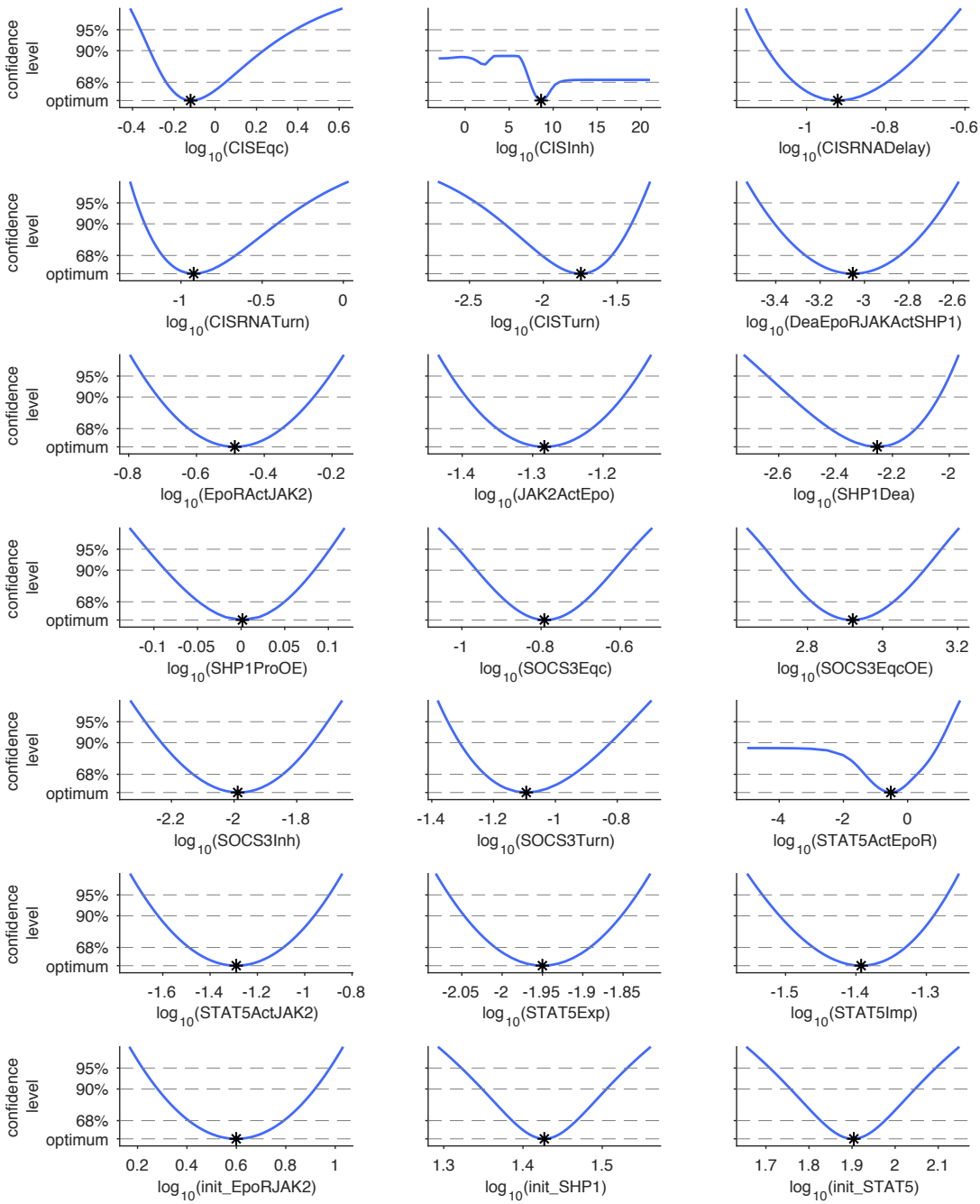

Figure S3 (related to Figure 2): Likelihood profiles of the pathway model with population-level data for all dynamic model parameters (blue lines). Black asterisks indicate the best fit and global optimum. Intersections of the likelihood profiles (blue solid lines) with the statistical thresholds for different confidence levels (gray dashed horizontal lines) indicate the profile likelihood-based confidence intervals. All parameters are identifiably with confidence levels of 68%. Only parameters CISInh and STAT5ActEpoR reveal practical non-identifiabilities for higher confidence levels. These non-identifiabilities could be resolved only by further measurements but they do not weaken the predictive power of the model as a unique optimum of the model parameters is found.

1.4 Figure S4

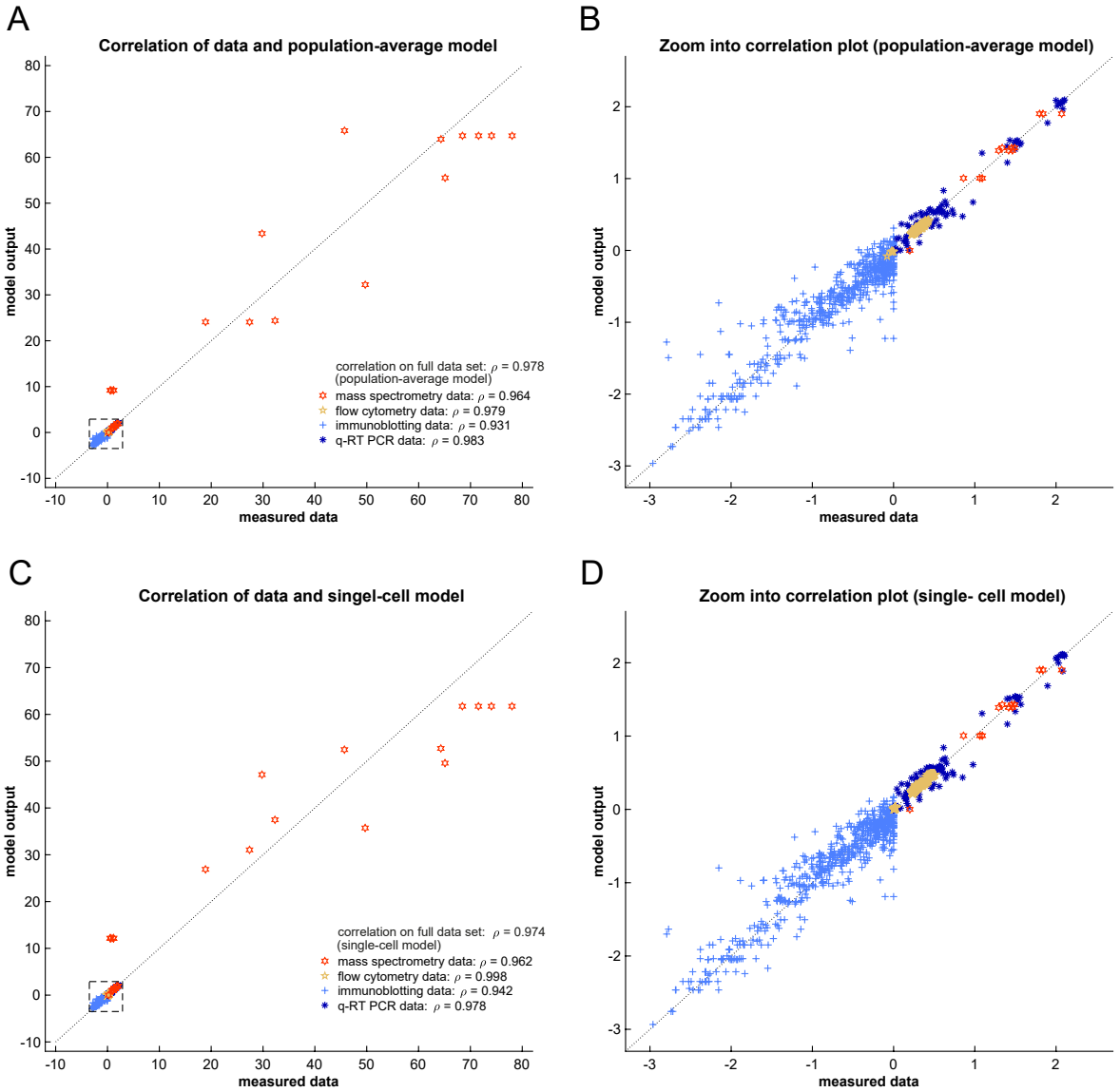

Figure S4 (related to Figure 4): Correlation of experimental data and model output. **(A)** Full data set for population-average model. Red hexagrams: mass spectrometry data (non-normalized, linear scale), yellow pentagrams: flow cytometry data (non-normalized, logicle scale), light blue plus signs: immunoblotting data (normalized, log-scale), deep blue asterisks: qRT-PCR data (non-normalized, log-scale). **(B)** Zoom into correlation plot for population-average model. **(C)** Full data set for single-cell model. **(D)** Zoom into correlation plot for single-cell model.

1.5 Figure S5

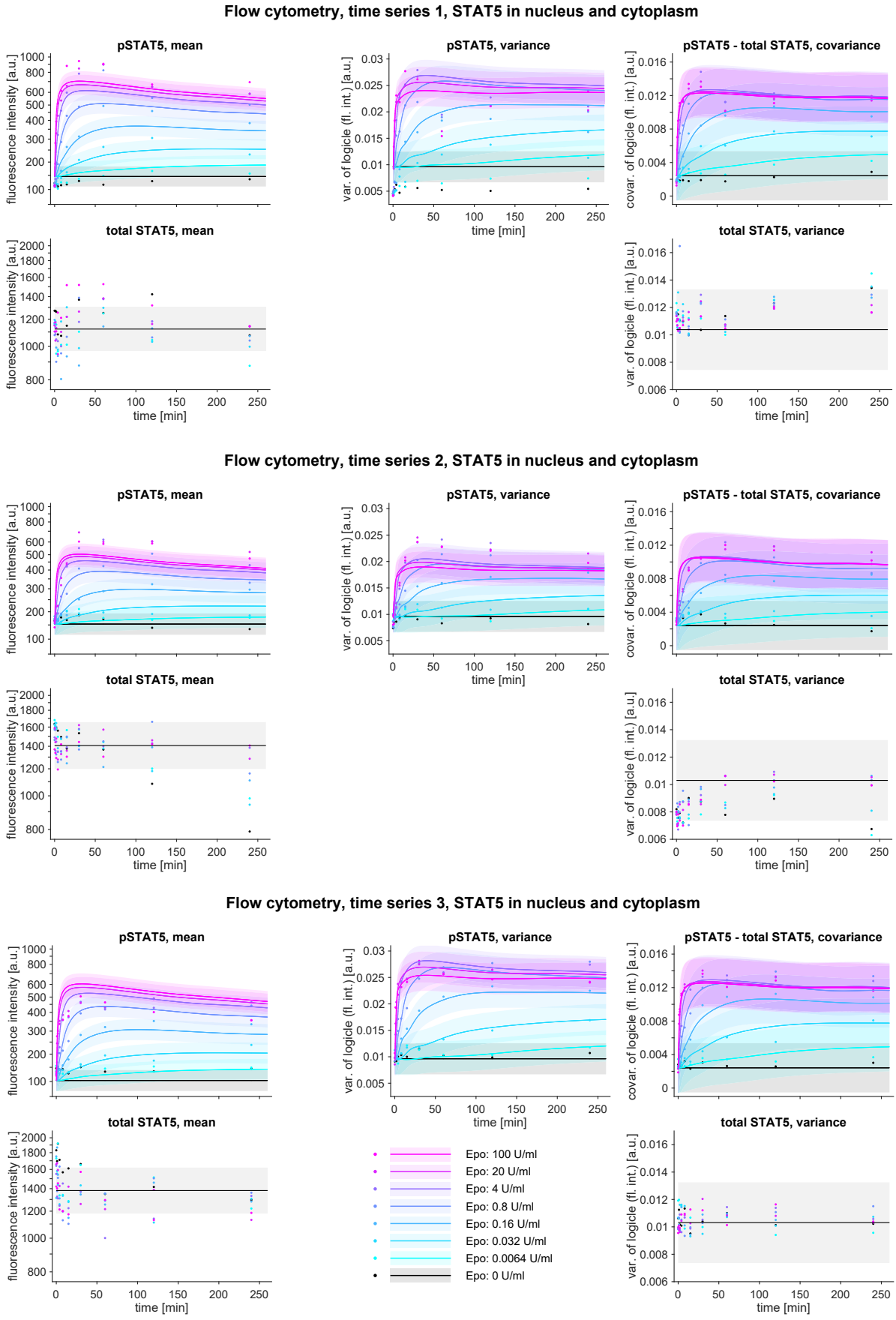
Flow cytometry, time series 1, STAT5 in nucleus and cytoplasm
pSTAT5, mean
pSTAT5, variance
pSTAT5 - total STAT5, covariance
total STAT5, mean
total STAT5, variance
Flow cytometry, time series 2, STAT5 in nucleus and cytoplasm
pSTAT5, mean
pSTAT5, variance
pSTAT5 - total STAT5, covariance
total STAT5, mean
total STAT5, variance
Flow cytometry, time series 3, STAT5 in nucleus and cytoplasm
pSTAT5, mean
pSTAT5, variance
pSTAT5 - total STAT5, covariance
total STAT5, mean
total STAT5, variance
fluorescence intensity [a.u.]
var. of logicle (fl. int.) [a.u.]
covar. of logicle (fl. int.) [a.u.]
time [min]
Epo: 100 U/ml
Epo: 20 U/ml
Epo: 4 U/ml
Epo: 0.8 U/ml
Epo: 0.16 U/ml
Epo: 0.032 U/ml
Epo: 0.0064 U/ml
Epo: 0 U/ml

Figure S5 (related to Figure 5): Flow-cytometry data and model fit for the selected single-cell model. Three data sets were measured for eight Epo doses (colors), using flow cytometry and time-resolved experiments. Each experiment shows time-courses of population means (left) of pSTAT5 (upper panel) and total STAT5 (lower panel), and time-course variances and covariance of both species plotted as correlation matrix trajectories (right).

1.6 Figure S6

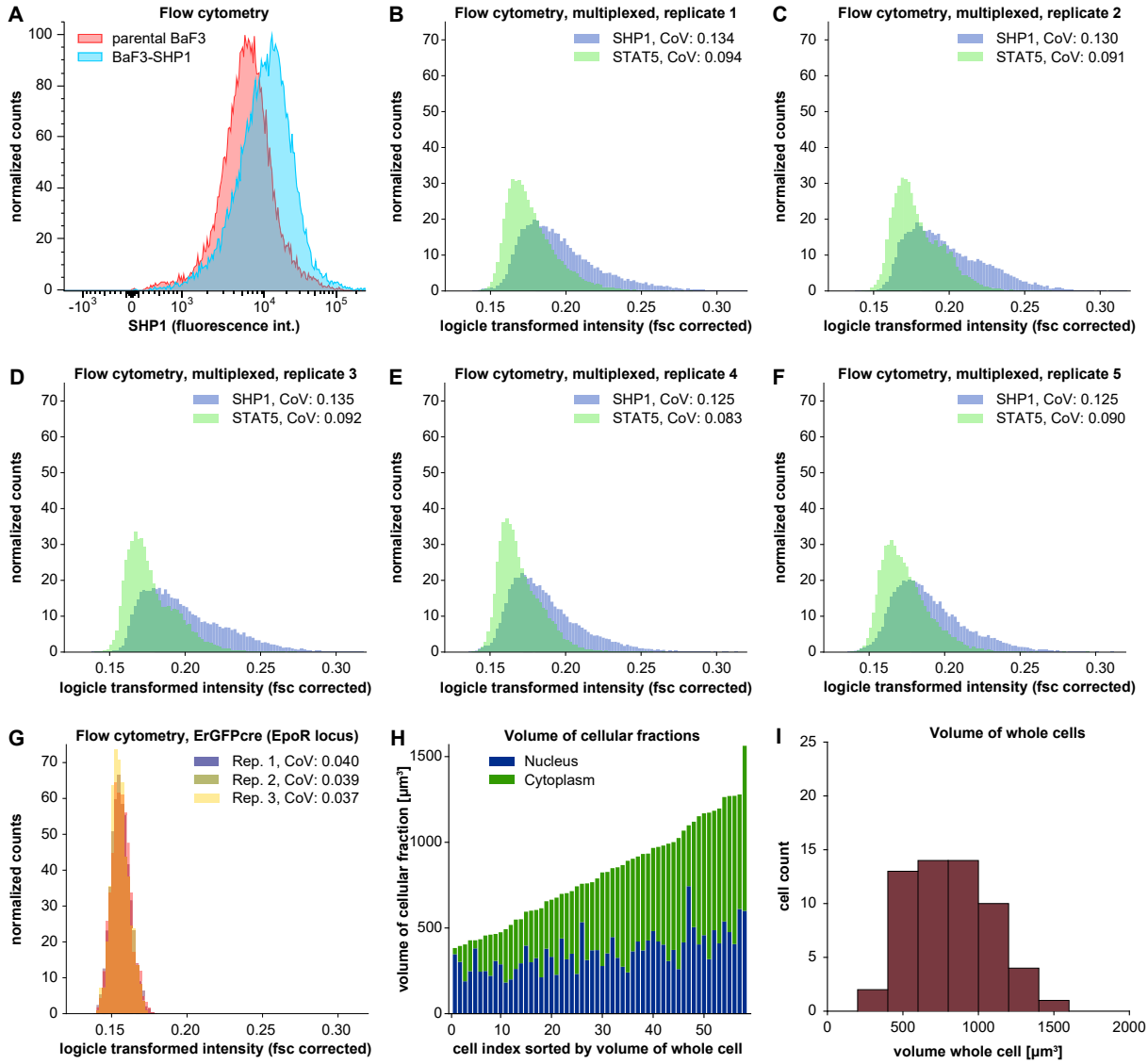

Figure S6 (related to Figure 6): Validation experiments on cell-to-cell variability of protein abundances by flow cytometry and of cytoplasmic and nuclear volumes by confocal microscopy and 3D reconstruction. **(A)** Flow cytometry of SHP1 was performed in parental BaF3 cells and in cells overexpressing SHP1 via a retroviral vector (BaF3-SHP1). **(B-G)** Flow cytometry was performed in unstimulated growth factor-depleted CFU-E cells. Measurement values were trans-formed to logicle scale, after being normalized with the respective front scatter (fsc) value. The normalization accounts for variable cell sizes and should reflect the actual concentrations of the measured proteins better than the raw measurement values. All measurement were transformed to logicle scale using the same hyperparameters, in order to ensure comparability of biological variability indicated as coefficient of variation (CoV). **(B-F)** Replicate measurements of multi-plexed SHP1-STAT5 flow cytometry. **(G)** Three replicate measurements of GFP, using a knock-in mouse model that expresses an GFPcre fusion protein controlled by the endogenous EpoR promoter (ErGFPcre) as a proxy for the actual Epo receptor. **(H)** Analysis of cytoplasmic and nuclear volumes from unstimulated growth factor-depleted CFU-E cells from by confocal microscopy and 3D reconstruction. Measured nucleus and cytoplasm volumes from n = 58 cells. **(I)** Distribution of whole cell volumes.

1.7 Figure S7

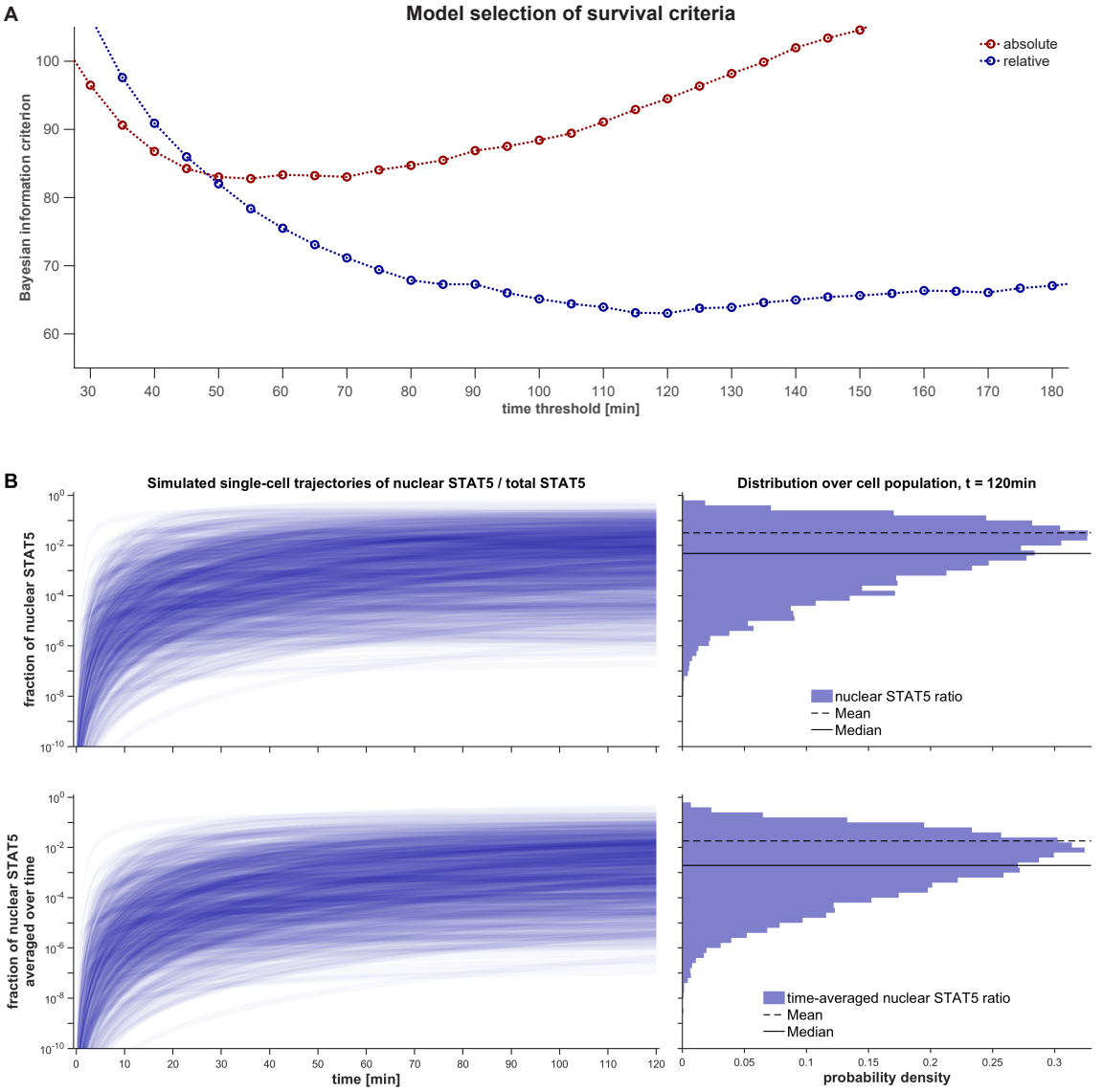

Figure S7 (related to Figure 7): Model simulations to link the amount of pSTAT5 in the nucleus to cell survival. **(A)** BIC results for model selection for different possible models of cell survival. pSTAT5 must be in the nucleus to ensure cell survival. An absolute criterion, i.e., the abundance of STAT5 in the nucleus (red) and a relative criterion, i.e., the percentage of a cell's STAT5 in the nucleus (blue), were compared against each other for different time intervals. Survival thresholds and offset parameters were fitted and the fit quality was compared. The relative criterion for a time interval of 120 minutes provided the best results.
(B) Trajectories (left panel) for an in-silico population of 10 000 cells at EC_{50}-dose of Epo, which show the fraction of pSTAT5 in the cell's nucleus (upper panel) and the time-average of this fraction from t = 0 to the current time (lower panel). The right panel shows the histograms over the population for the two quantities at t = 120 min, which demonstrate the log-normal distribution of the survival signal. The median in the lower right panel represents the survival threshold.